

A topology optimisation framework to design test specimens for one-shot identification or discovery of material models

Saeid Ghoulia, Moritz Flaschel^a, Siddhant Kumar^b, Laura De Lorenzis^{a,*}

^a*Department of Mechanical and Process Engineering, ETH Zürich, 8092 Zürich, Switzerland*

^b*Department of Materials Science and Engineering, Delft University of Technology, 2628 CD Delft, The Netherlands*

Abstract

The increasing availability of full-field displacement data from imaging techniques in experimental mechanics is determining a gradual shift in the paradigm of material model calibration and discovery, from using several simple-geometry tests towards a few, or even one single test with complicated geometry. The feasibility of such a “one-shot” calibration or discovery heavily relies upon the richness of the measured displacement data, i.e., their ability to probe the space of the state variables and the stress space (whereby the stresses depend on the constitutive law being sought) to an extent sufficient for an accurate and robust calibration or discovery process. The richness of the displacement data is in turn directly governed by the specimen geometry. In this paper, we propose a density-based topology optimisation framework to optimally design the geometry of the target specimen for calibration of an anisotropic elastic material model. To this end, we perform automatic, high-resolution specimen design by maximising the robustness of the solution of the inverse problem, i.e., the identified material parameters, given noisy displacement measurements from digital image correlation. We discuss the choice of the cost function and the design of the topology optimisation framework, and we analyse a range of optimised topologies generated for the identification of isotropic and anisotropic elastic responses.

Keywords: Optimised specimen geometry, topology optimisation, constitutive law calibration, one-shot discovery.

1. Introduction

Characterising the mechanical behaviour of materials typically requires multiple tests. For instance, fully characterising the linear elastic behaviour of a planar orthotropic material (such as a composite lamina) typically demands at least three separate experiments (Tsai, 1965; Acosta-Flores and Eraña-Díaz, 2024); these could be, for instance, a longitudinal tensile test (measuring longitudinal and transverse strains simultaneously), a transverse tensile test, and an in-plane shear test. Also, traditional mechanical testing involves measurements with contact sensors such as strain gauges or displacement transducers, providing local experimental data only. The advent of advanced full-field measurement techniques such as digital image correlation (DIC) and digital volume correlation (DVC) has revolutionised the field of material law characterisation by opening up the perspective of fully characterising material behaviour with one single test (Guélon et al., 2009; Fu et al., 2020). In this new context, the optimal design of the target specimen is of utmost importance. A review paper by Pierron and Grédiac (2021) denotes this paradigm as “material testing 2.0”.

During the last decades, different groups of researchers have dealt with the specimen design problem suited for parameter identification via full-field measurements. As follows, we briefly highlight the major concepts and methodologies, focusing only on automatic (i.e., optimisation-based) approaches. Many studies have dealt with shape optimisation techniques to optimise the geometry of a pre-selected topology parametrised with a few variables. Different cost functions have been used for different classes of constitutive laws. In the context of orthotropic materials, Grédiac and Pierron (1998) aimed at equal co-existence of different strain components in the test specimen. Pierron et al. (2007)

*Corresponding author

Email address: ldelorenzis@ethz.ch (Laura De Lorenzis)

targeted maintaining the balance between the sensitivities to noise for the identification of the different stiffness components. [Gu and Pierron \(2016\)](#) accounted for the full identification process, thus optimising the DIC metrological parameters in addition to geometrical variables. The cost function was defined as the sum of systematic and random errors when calibrating the orthotropic stiffness components. Such a cost definition depends on the reference (i.e., ground-truth) material parameters. In the context of elastoplasticity, [Souto et al. \(2015\)](#) put forward the definition of a heterogeneity indicator (combining the standard deviation, range, maximum and average of different strain states) which could assess the suitability of a test specimen for sheet metal testing. The heterogeneity indicator was then employed in [Souto et al. \(2016\)](#) to design a butterfly-shaped specimen. [Bertin et al. \(2016\)](#) minimised the uncertainty in the parameter identification process by maximising the minimum eigenvalue of the Hessian matrix encountered in the finite element model updating (FEMU) approach. [Chapelier et al. \(2022\)](#) followed a similar approach and proposed a spline-based shape optimisation with special constraints to prevent excessive mesh distortion and load increase in a two-step shape optimisation, involving remeshing in between. [Zhang et al. \(2022\)](#) and [Conde et al. \(2023\)](#) employed the heterogeneity indicator proposed by [Souto et al. \(2015\)](#) in their cost functions, and confirmed that the initial configuration of the geometry has a strong influence on the final optimised design. More recently, [Tung and Li \(2024\)](#) devised a cost function quantifying the spread of data points in the deviatoric plane, while [Ihuoenyi et al. \(2024\)](#) utilised the information entropy concept to quantify the heterogeneity of the stress data points in the space of stress-triaxiality versus Lode angle parameter.

Another stream of research has employed topology optimisation techniques to automatically design optimal test specimens for constitutive parameter calibration facilitated by DIC measurements. Within the popular framework of density-based topology optimisation, the design variables are the virtual densities which designate the existence of void or material in each element of a finite element (FE) mesh ([Bendsøe, 1989](#)). Also in this stream, different cost formulations have been proposed. For orthotropic materials, [Chamoine et al. \(2020\)](#) followed a similar strategy to [Bertin et al. \(2016\)](#) to minimise the uncertainty in the parameter identification process. Owing to the computational cost associated with numerical gradient calculation, only coarse-resolution topologies including grey scales were generated. [Almeida et al. \(2020\)](#) employed the sum of fractions of the specimen surface undergoing certain principal stress states as a heterogeneity function, which was then used in a multi-objective optimisation setup together with the compliance to maintain sufficient stiffness in the designed specimen. The final designs had low resolutions, contained grey scales, and were difficult to realise and manufacture. The weights balancing the multi-objective optimisation problem were adjusted heuristically, while they were recognised to highly influence the output. [Barroqueiro et al. \(2020\)](#) adopted the concept of compliant mechanisms and proposed the ratio between the output and input displacements (of the mechanism with linear elastic response) as the cost function. Through a two-stage algorithm, the authors first produced a large number of heterogeneous designs, and then ranked them using a performance indicator (favouring equal co-existence of different deformation modes) while assuming an elastoplastic response. The best topology underwent a manual redesign to ensure smooth outer boundaries. [Gonçalves et al. \(2023\)](#) improved the original framework proposed in [Barroqueiro et al. \(2020\)](#) by considering an additional, outer optimisation loop (leading to a two-level optimisation framework) which sought an optimal design domain configuration by changing parameters such as aspect ratio and material volume fraction. The authors performed numerous preliminary studies to define suitable bounds for the configurational parameters such that the heterogeneously designed specimen does not fail prematurely (i.e., prior to plasticity). The design strategy remained indirect and two-step while requiring expertise in selecting the parameter bounds and (dis-)approving the generated designs.

The above short review reveals some gaps in the current state of the art. Shape optimisation approaches, while leading to much faster computations, require significant expertise in material testing for the initial selection of a suitable topology. On the other hand, when employing topology optimisation, the need to reduce the computational cost (due to the exploding number of design variables and possibly the employment of finite differences for sensitivity calculation) often results in low-resolution or grey-scale-diluted topologies. Two-step processes require manual intervention. Also, it seems that not much attention has been paid so far to global convergence (i.e., mesh independence) of the optimised topologies to ensure their consistency as the FE discretisation of the design domain is refined. This property indicates the appropriateness of the cost definition for driving a stable optimisation process until convergence, and confirms resilience against small perturbations of the initialisation. Lastly, in the case of multi-objective optimisation (e.g. to improve manufacturability), the determination of weight factors balancing the different cost terms has been found to greatly impact the optimisation outcome. Yet, a non-systematic heuristic approach has been adopted.

In this work, we propose a new topology optimisation framework for robust identification of constitutive param-

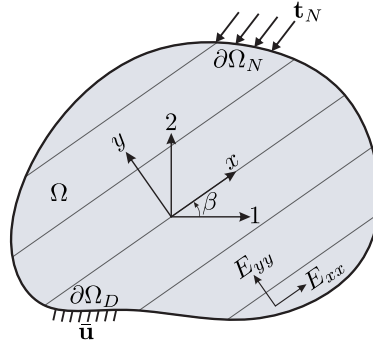


Figure 1: The boundary value problem of plane deformation for the case of an orthotropic elastic medium. The x - y coordinate system aligns with the anisotropy orientation β indicated by hatches and measured counterclockwise from the reference coordinates 1-2.

eters. We employ the density-based topology optimisation approach, and choose a high resolution to allow for great flexibility in the specimen design. Through filtering techniques, we provide binary, black-and-white designs. The cost function for the topology optimisation problem is defined based on our recently proposed material model discovery approach denoted as EUCLID (Flaschel et al., 2021), is independent of the ground-truth material parameters and targets the stability of the identification problem equations. We compute the sensitivities analytically and in a vectorised fashion. Moreover, we investigate and prove the global convergence of the optimised topologies. To account for manufacturability and avoid possible weak regions in the specimen design, we employ the concept of robust topology optimisation which automates the redesigning process by a three-field projection filtering. We present the resulting optimised topologies for a range of linear elastic isotropic and orthotropic materials and assess their performance in terms of error in parameter identification. This paper is organised as follows. In Section 2 we formulate the constitutive parameter identification framework within anisotropic linear elasticity, which provides the basis for our topology optimisation framework in Section 3. Section 4 presents the main results and also discusses the concepts of global and local convergence. We conclude the paper in Section 5.

2. Parameter identification framework

In this section, we establish the system of equations leading to the unknown constitutive parameters. The input data consist of a (noisy) deformation field captured by DIC from the surface of a target specimen. We consider a deformable solid occupying the 2D domain Ω with boundary $\partial\Omega$ (Fig. 1). Assuming small deformations and neglecting body forces, the principle of virtual work reads

$$\int_{\Omega} \boldsymbol{\sigma} : \nabla(\delta \mathbf{u}) dA - \int_{\partial\Omega_N} \bar{\mathbf{t}}_N \cdot \delta \mathbf{u} ds \stackrel{!}{=} 0, \quad (1)$$

where \mathbf{u} is the displacement field satisfying Dirichlet boundary conditions (i.e., $\mathbf{u} = \bar{\mathbf{u}}$ on $\partial\Omega_D$), the virtual displacement $\delta \mathbf{u}$ is sufficiently regular and satisfies homogeneous Dirichlet boundary conditions (i.e., $\delta \mathbf{u} = \mathbf{0}$ on $\partial\Omega_D$) but is otherwise arbitrary, $\boldsymbol{\sigma}$ is the Cauchy stress tensor, and $\bar{\mathbf{t}}_N$ is the traction applied on the Neumann portion of the boundary $\partial\Omega_N$. The FE approximation of Eq. (1) defined over the domain Ω^h discretised into n_e elements (each with domain Ω_e) reads

$$\sum_{e=1}^{n_e} \int_{\Omega_e} \boldsymbol{\sigma}_e^h : \nabla(\delta \mathbf{u}_e^h) dA - \sum_{e: \partial\Omega_e \subset \partial\Omega_N^h} \int_{\partial\Omega_e} \bar{\mathbf{t}}_{N_e} \cdot \delta \mathbf{u}_e^h ds \stackrel{!}{=} 0, \quad (2)$$

with superscript h and subscript e denoting FE discretisation and element-related quantities, respectively. For discretisation we adopt standard isoparametric FEs with linear shape functions $N^a(\boldsymbol{\xi})$, i.e.

$$\mathbf{u}_e^h(\boldsymbol{\xi}) = \sum_{a=1}^{n_{n,e}} N^a(\boldsymbol{\xi}) \mathbf{u}_e^a, \quad \delta \mathbf{u}_e^h(\boldsymbol{\xi}) = \sum_{a=1}^{n_{n,e}} N^a(\boldsymbol{\xi}) \delta \mathbf{u}_e^a, \quad \mathbf{x}_e^h(\boldsymbol{\xi}) = \sum_{a=1}^{n_{n,e}} N^a(\boldsymbol{\xi}) \mathbf{x}_e^a, \quad (3)$$

where superscript a refers to nodal quantities, $n_{n,e}$ is the number of nodes of element e , and parent space coordinates ξ are related to \mathbf{x} through the Jacobian $\mathbf{J}_e = \partial \mathbf{x}_e^f / \partial \xi$. We collect the nodal displacements in $\mathbf{U}_e \in \mathbb{R}^{|\mathcal{D}_e|}$, where $\mathcal{D}_e = \{(a, i) : a = 1, \dots, n_{n,e}; i = 1, 2\}$ designates the collection of all the degrees of freedom (DOFs) of element e , and accordingly arrange the shape functions N^a in the matrix $\mathbf{N} \in \mathbb{R}^{|\mathcal{D}_e| \times 2}$ and their gradients $\nabla_{\mathbf{x}} \mathbf{N} = \mathbf{J}_e^{-T} \nabla_{\xi} \mathbf{N}$ as the transpose of $\mathbf{B}_e \in \mathbb{R}^{3 \times |\mathcal{D}_e|}$. Rewriting Eq. (2) with integration over the parent element domain Ω_{\square} gives

$$\delta \mathbf{U}^T \left(\sum_{e=1}^{n_e} \underbrace{\int_{\Omega_{\square}} \mathbf{B}_e^T(\xi) \hat{\sigma}_e^f(\xi) \det(\mathbf{J}_e(\xi)) dA_{\square}}_{\mathbf{F}_{int,e}} - \sum_{e: \partial \Omega_e \subset \partial \Omega_N^f} \underbrace{\int_{\partial \Omega_{\square}} \mathbf{N}^T(\xi) \bar{\mathbf{t}}_{N_e} j_e^s ds_{\square}}_{\mathbf{F}_{ext,e}} \right) \stackrel{!}{=} 0, \quad (4)$$

where we use Voigt notation for the stress $\hat{\sigma}_e^f = [\sigma_{11}, \sigma_{22}, \tau_{12}]^T$, j_e^s is the length Jacobian for the boundary mapping between parent and physical element, and we introduce the assembly operation $\mathbf{U} = \bigcup_{e=1}^{n_e} \mathbf{U}_e$ with $\mathbf{U} \in \mathbb{R}^{|\mathcal{D}|}$, \mathcal{D} as the set of all nodal DOFs, i.e., $\mathcal{D} = \{(a, i) : a = 1, \dots, n_n; i = 1, 2\}$, and n_n as the total number of nodes. In Eq. (4), the two integrals represent the element internal and external force vectors, $\mathbf{F}_{int,e}, \mathbf{F}_{ext,e} \in \mathbb{R}^{|\mathcal{D}_e|}$, respectively. Assuming now anisotropic linear elasticity, we can express the Cauchy stress vector $\hat{\sigma}_e^f$ as a function of the strain vector, also expressed in Voigt notation as $\hat{\epsilon}_e^f = [\epsilon_{11}, \epsilon_{22}, \gamma_{12}]^T = \mathbf{B}_e \mathbf{U}_e$, in two equivalent formats as follows

$$\hat{\sigma}_e^f = \tilde{\rho}_e^{\text{phys}} \begin{bmatrix} D_{11} & D_{12} & D_{16} \\ \text{sym.} & D_{22} & D_{26} \\ & & D_{66} \end{bmatrix} \begin{Bmatrix} \epsilon_{11} \\ \epsilon_{22} \\ \gamma_{12} \end{Bmatrix} = \tilde{\rho}_e^{\text{phys}} \underbrace{\begin{bmatrix} \epsilon_{11} & \epsilon_{22} & \gamma_{12} & 0 & 0 & 0 \\ 0 & \epsilon_{11} & 0 & \epsilon_{22} & \gamma_{12} & 0 \\ 0 & 0 & \epsilon_{11} & 0 & \epsilon_{22} & \gamma_{12} \end{bmatrix}}_{\hat{\epsilon}_e^f} \underbrace{\begin{Bmatrix} D_{11} \\ D_{12} \\ D_{16} \\ D_{22} \\ D_{26} \\ D_{66} \end{Bmatrix}}_{\boldsymbol{\theta}} = \tilde{\rho}_e^{\text{phys}} \hat{\epsilon}_e^f \boldsymbol{\theta}. \quad (5)$$

Here, the factor $\tilde{\rho}_e^{\text{phys}}$ is the modified physical density of element e in the context of topology optimisation, to be better specified later. In the second equality of Eq. (5), the strain components are cast in the matrix $\hat{\epsilon}_e^f \in \mathbb{R}^{3 \times n_f}$ and the elements of the elasticity matrix \mathbf{D} are gathered in the vector of the unknown material parameters $\boldsymbol{\theta} \in \mathbb{R}^{n_f}$, where $n_f = 6$. Employing Eq. (5) in the definition of the element internal force vector from Eq. (4) gives

$$\mathbf{F}_{int,e} = \tilde{\rho}_e^{\text{phys}} \underbrace{\left(\int_{\Omega_{\square}} \mathbf{B}_e^T(\xi) \hat{\epsilon}_e^f(\xi) \det(\mathbf{J}_e(\xi)) dA_{\square} \right)}_{\mathbf{A}_e} \boldsymbol{\theta} = \tilde{\rho}_e^{\text{phys}} \mathbf{A}_e \boldsymbol{\theta}, \quad (6)$$

where we have assumed spatial invariance of the material parameters $\boldsymbol{\theta}$ and designated the element integral by $\mathbf{A}_e \in \mathbb{R}^{|\mathcal{D}_e| \times n_f}$. Using n_{gp} Gauss quadrature points per parametric direction with coordinates (ξ_i, η_j) ($i, j = 1, \dots, n_{\text{gp}}$) and corresponding weights w_i, w_j , \mathbf{A}_e is computed as

$$\mathbf{A}_e(\hat{\epsilon}_e^f(\mathbf{U}_e)) = \int_{\Omega_{\square}} \mathbf{B}_e^T(\xi) \hat{\epsilon}_e^f(\xi) \det(\mathbf{J}_e(\xi)) dA_{\square} \approx \sum_{i=1}^{n_{\text{gp}}} \sum_{j=1}^{n_{\text{gp}}} \mathbf{B}_e^T(\xi_i, \eta_j) \hat{\epsilon}_e^f(\xi_i, \eta_j) \det(\mathbf{J}_e(\xi_i, \eta_j)) \times w_i \times w_j. \quad (7)$$

Row-wise assembly over $\mathbf{F}_{int,e}$ from Eq. (6) then gives the global matrix

$$\mathbf{A}_{\text{glob}}(\boldsymbol{\rho}^{\text{phys}}, \mathbf{U}) = \bigcup_{e=1}^{n_e} \tilde{\rho}_e^{\text{phys}} (\rho_e^{\text{phys}}) \mathbf{A}_e(\mathbf{U}_e). \quad (8)$$

The dependence of $\mathbf{A}_{\text{glob}} \in \mathbb{R}^{|\mathcal{D}| \times n_f}$ on the vector of element physical densities $\boldsymbol{\rho}^{\text{phys}} \in \mathbb{R}^{n_e}$ and on \mathbf{U} will be exploited in Section 3.2. Both \mathbf{A}_{glob} and \mathbf{A}_e have unit of length.

The set of all DOFs \mathcal{D} consists of two subsets, namely the free and fixed (i.e., Dirichlet boundary) DOFs: $\mathcal{D}^{\text{free}} \subseteq \mathcal{D}$ and $\mathcal{D}^{\text{fix}} = \mathcal{D} \setminus \mathcal{D}^{\text{free}}$. The equilibrium equation for the free DOFs can be obtained from Eq. (4) using Eq. (8):

$$\mathbf{A}_{\text{glob}}^{\text{free}} \boldsymbol{\theta} \stackrel{!}{=} \mathbf{b}_{\text{glob}}^{\text{free}}, \quad (9)$$

where $\mathbf{A}_{\text{glob}}^{\text{free}} \in \mathbb{R}^{|\mathcal{D}^{\text{free}}| \times n_f}$ and $\mathbf{b}_{\text{glob}}^{\text{free}} \in \mathbb{R}^{|\mathcal{D}^{\text{free}}|}$. Here, we note that $\mathbf{b}_{\text{glob}}^{\text{free}}$ contains the integrated global traction forces over the Neumann boundary (in a displacement-controlled setting, $\mathbf{b}_{\text{glob}}^{\text{free}} = \mathbf{0}$).

For the fixed DOFs, the internal force from the material must balance out with the reaction force. Practically, the reaction force is not known at every fixed DOF; rather, it is only the sum of the reaction forces $\bar{\mathbf{R}}^s$ that can be measured experimentally at certain subsets of the fixed DOFs denoted as $\mathcal{D}^{\text{fix},s}$ ($s = 1, \dots, n_s$; $\cup_{s=1}^{n_s} \mathcal{D}^{\text{fix},s} \subseteq \mathcal{D}^{\text{fix}}$; $\mathcal{D}^{\text{fix},s} \cap \mathcal{D}^{\text{fix},t} = \emptyset$ for $s \neq t$). The force balance equation for each subset s can thus be written as

$$\sum_{\mathcal{D} \subset \mathcal{D}^{\text{fix},s}} \mathbf{A}_{\text{glob}}^{\text{fix},s} \boldsymbol{\theta} = \bar{\mathbf{R}}^s. \quad (10)$$

Note that each subset contains DOFs corresponding to displacement components only in one direction. The collection of these individual equations for all n_s subsets of the fixed DOFs will then provide us with

$$\mathbf{A}_{\text{glob}}^{\text{fix}} \boldsymbol{\theta} \stackrel{!}{=} \mathbf{b}_{\text{glob}}^{\text{fix}}, \quad (11)$$

wherein $\mathbf{A}_{\text{glob}}^{\text{fix}} \in \mathbb{R}^{n_s \times n_f}$ and $\mathbf{b}_{\text{glob}}^{\text{fix}} \in \mathbb{R}^{n_s}$. Note that, in a uniaxial testing setup, reaction forces are known only at the top and bottom fixed edges of the specimen (where they are equal and opposite), therefore $n_s = 2$.

Equations (9) and (11) are systems of linear equations which must be satisfied simultaneously by the solution $\boldsymbol{\theta}$. Therefore, we combine the two sets of equations by concatenating them vertically and defining $\mathbf{A} \in \mathbb{R}^{(|\mathcal{D}^{\text{free}}| + n_s) \times n_f}$ and $\mathbf{b} \in \mathbb{R}^{|\mathcal{D}^{\text{free}}| + n_s}$ as

$$\mathbf{A} = \sqrt{\lambda_q} [\mathbf{A}_{\text{glob}}^{\text{free}}; \sqrt{\lambda_r} \mathbf{A}_{\text{glob}}^{\text{fix}}]; \quad \mathbf{b} = \sqrt{\lambda_q} [\mathbf{b}_{\text{glob}}^{\text{free}}; \sqrt{\lambda_r} \mathbf{b}_{\text{glob}}^{\text{fix}}]. \quad (12)$$

Factor $\sqrt{\lambda_r}$ is used to balance the contribution of the fixed and free DOFs in the system of equations, whereas factor $\sqrt{\lambda_q}$ accounts for mesh convergence, see [Appendix A](#) for details. The final equilibrium equation reads

$$\mathbf{A} \boldsymbol{\theta} \stackrel{!}{=} \mathbf{b}. \quad (13)$$

Note that \mathbf{A} is a purely kinematic quantity, with dimension of a length, which encodes information only on the geometry, loading configuration and boundary conditions, while the material properties are contained in $\boldsymbol{\theta}$. Since $|\mathcal{D}^{\text{free}}| + n_s \gg n_f$, Eq. (13) is over-determined and can be solved in a least squares sense by

$$\mathbf{A}^{\text{eqb}} \boldsymbol{\theta} \stackrel{!}{=} \mathbf{b}^{\text{eqb}}, \quad (14)$$

with

$$\mathbf{A}^{\text{eqb}} = \mathbf{A}^T \mathbf{A} = \lambda_q \left((\mathbf{A}_{\text{glob}}^{\text{free}})^T \mathbf{A}_{\text{glob}}^{\text{free}} \right) + \lambda_r \left(\mathbf{A}_{\text{glob}}^{\text{fix}}^T \mathbf{A}_{\text{glob}}^{\text{fix}} \right) \in \mathbb{R}^{n_f \times n_f}, \quad (15a)$$

$$\mathbf{b}^{\text{eqb}} = \mathbf{A}^T \mathbf{b} = \lambda_q \left((\mathbf{A}_{\text{glob}}^{\text{free}})^T \mathbf{b}_{\text{glob}}^{\text{free}} \right) + \lambda_r \left(\mathbf{A}_{\text{glob}}^{\text{fix}}^T \mathbf{b}_{\text{glob}}^{\text{fix}} \right) \in \mathbb{R}^{n_f}, \quad (15b)$$

where the symmetric positive definite matrix \mathbf{A}^{eqb} and the right-hand side \mathbf{b}^{eqb} have dimensions of a square length and a force, respectively. A well-known result in numerical analysis ([Ascher and Greif, 2011](#)) gives the following estimate

$$\frac{\|\delta \boldsymbol{\theta}\|_2}{\|\boldsymbol{\theta}\|_2} \leq \kappa_2(\mathbf{A}^{\text{eqb}}) \frac{\|\delta \mathbf{b}^{\text{eqb}}\|_2}{\|\mathbf{b}^{\text{eqb}}\|_2}, \quad (16)$$

where $\delta \mathbf{b}^{\text{eqb}}$ and $\delta \boldsymbol{\theta}$ are the perturbations (i.e., noise) in the problem and the induced error in the solution, respectively, and

$$\kappa_2(\mathbf{A}^{\text{eqb}}) = \left\| \mathbf{A}^{\text{eqb}} \right\|_2 \left\| \mathbf{A}^{\text{eqb}}^{-1} \right\|_2 \quad (17)$$

is the 2-norm condition number of \mathbf{A}^{eqb} . This inequality indicates that the ℓ_2 -error magnification from the problem to the solution is bounded by $\kappa_2(\mathbf{A}^{\text{eqb}})$. In other words, it is the condition number which governs the stability of the solution $\boldsymbol{\theta}$ upon perturbation in the problem. Hence, in order to minimise the uncertainty/maximise the robustness of the constitutive law identification against the noise in the deformation data, $\kappa_2(\mathbf{A}^{\text{eqb}})$ should be minimised. As discussed earlier, \mathbf{A}^{eqb} is a purely kinematic quantity which depends, among others, on the geometry of the domain, i.e., the test specimen used for material testing. This fact inspires the possibility of defining an appropriate cost function targeting the minimisation of $\kappa_2(\mathbf{A}^{\text{eqb}})$ and utilising it in an optimisation framework to optimally design the test specimen.

3. Topology optimisation framework

Topology optimisation seeks to find the best material layout in a design domain in order to minimise a certain cost function given a number of design constraints. Among different well-established approaches (Sigmund and Maute, 2013), we employ the density-based topology optimisation approach (Bendsøe, 1989), where the design variables are the virtual densities assigned to the FEs in the discretised domain. The virtual densities can acquire values between zero and one, representing the (non-)existence of material. In the following, we describe the design domain and define our choice of the cost function.

3.1. Setup

Fig. 2b shows the rectangular domain, with dimensions L_X and L_Y , and the Dirichlet boundary conditions corresponding to a displacement-controlled tensile test with imposed displacement $\bar{u} = 0.005 \times L_Y$ uniformly applied on the top edge. Note that in principle it would be possible to consider multiple load cases and optimise the topology for all the considered load cases. Herein, we stick to the uniaxial loading setup which is very common in the experimental practice. The black frame around the design domain is the so-called *passive* region whose density values are kept fixed at 1 with no changes allowed, while the inner grey area is open to change and optimisation. We always account for this passive frame around the design domain to ensure the preservation of the gripping areas at the top and bottom of the specimen (where the testing machine holds the specimen, i.e., Dirichlet boundaries), and to prevent the formation of holes and narrow strips of material in the proximity of the edges (which can be prone to premature failure upon loading and are often deemed inapplicable for DIC measurements). While the use of a fixed outer frame introduces small limitations to the design space, our approach remains highly versatile, as we will demonstrate below.

3.2. Choice of the cost function

In order to mitigate the error in the calibration of the constitutive parameters and enhance their stability in the presence of noise, we aim to utilise topology optimisation to automatically design the topology of the test specimen so as to minimise the 2-norm condition number $\kappa_2(\mathbf{A}^{\text{eqb}})$ in Eq. (17). A more general candidate is the p -norm condition number κ_p defined as

$$\kappa_p(\mathbf{A}^{\text{eqb}}) = \left\| \mathbf{A}^{\text{eqb}} \right\|_p \left\| \mathbf{A}^{\text{eqb}-1} \right\|_p, \quad (18)$$

where

$$\left\| \mathbf{A}^{\text{eqb}} \right\|_p = \left(\sum_{i=1}^{n_f} \sum_{j=1}^{n_f} |A_{ij}^{\text{eqb}}|^p \right)^{\frac{1}{p}}, \quad (19)$$

with $p > 2$, is the p -norm of matrix \mathbf{A}^{eqb} . The bounds reported in Appendix B.3 show that the minimisation of κ_p induces the minimisation of κ_2 . Hence, a candidate cost function is

$$\text{cost}_{\text{alt},1}(\boldsymbol{\rho}^{\text{phys}}, \mathbf{U}) = \frac{\kappa_p(\mathbf{A}^{\text{eqb}}(\boldsymbol{\rho}^{\text{phys}}, \mathbf{U}))^p}{\kappa_p(\mathbf{A}_{\text{@init.}}^{\text{eqb}})^p}, \quad (20)$$

which is continuously differentiable away from zero. Based on our numerical experiments reported later, $p \geq 8$ leads to a stable topology optimisation process with gradual topology updates, whereas $p < 8$ behaves rather unstably and causes abrupt topology changes. Division by the initial value $\kappa_p(\mathbf{A}_{\text{@init.}}^{\text{eqb}})^p$ normalises the cost function and brings more stability to the optimisation process with more gradual topology updates. An advantage of optimising a condition number (be it κ_2 , κ_p with $p \neq 2$ or condition numbers in other norms) is the insensitivity to the strain level induced in the specimen; this is owing to the fact that the condition number comprises the product of the norms of the matrix and the matrix inverse, hence cancelling out the strain magnitude. This feature enables the specimen design not to solely rely on high-strain concentration scenarios, but rather promote milder strain variations across the specimen and yet improve the identifiability of the material parameters. Inspired by Chamoin et al. (2020) and Zhang et al. (2022), we evaluate another possible cost function, namely, $1/\det(\mathbf{A}^{\text{eqb}})$, which is also continuously differentiable:

$$\text{cost}(\boldsymbol{\rho}^{\text{phys}}, \mathbf{U}) = \frac{\det(\mathbf{A}_{\text{@init.}}^{\text{eqb}})}{\det(\mathbf{A}^{\text{eqb}}(\boldsymbol{\rho}^{\text{phys}}, \mathbf{U}))}, \quad (21)$$

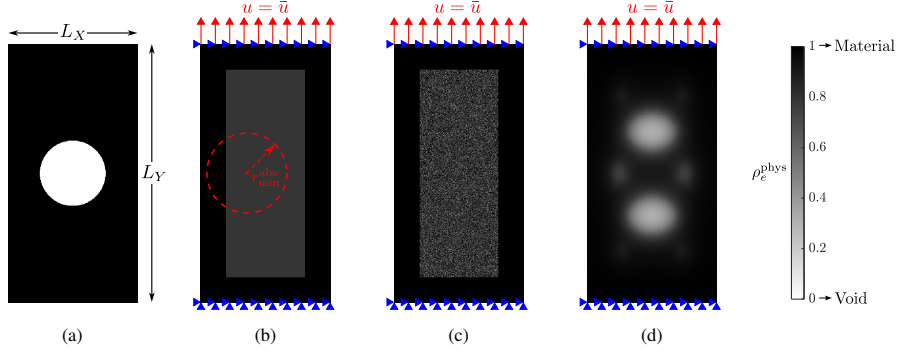


Figure 2: (a) Designation of 0 (void) and 1 (material) densities as well as domain dimensions; (b) even, (c) random, and (d) interim-valued initialisations of the domain; Dirichlet boundary conditions resembling the uniaxial tensile test are schematised. The absolute filtering radius r_{\min}^{abs} is also visualised in figure (b).

where the initial value, i.e., $\det(\mathbf{A}_{\text{init.}}^{\text{eqb}})$, non-dimensionalises the cost and alleviates the dependence on the strain level (i.e., the imposed external displacement). The minimisation of this cost drives the matrix away from singularity, but a priori does not necessarily result in the minimisation of the condition number (Ascher and Greif, 2011). In our numerical experiments, adopting these and a few more options for the cost function (see also Appendix B), we found $1/\det(\mathbf{A}^{\text{eqb}})$ to give the best performance, produce topologies with smoother boundaries, and drive the topology to a low condition number. In Section 4.1 we provide some comparisons between results obtained with Eqs. (20) and (21).

3.3. Density-based topology optimisation

We employ density-based topology optimisation (Bendsøe, 1989; Andreassen et al., 2011), where the design variables are the element densities ρ_e listed in the vector $\boldsymbol{\rho} \in \mathbb{R}^{n_e}$. Here, $\rho_e = 0$ and $\rho_e = 1$ respectively denote no material, i.e., void, and full material, colour-coded as white and black (see Fig. 2a). The intermediate densities, i.e. $0 < \rho_e < 1$, correspond to different shades of grey. In Appendix C we elaborate upon the transformation of ρ_e to ρ_e^{phys} through *filtering* which maps intermediate densities to either 0 or 1 to culminate in a physically realisable topology. With the mentioned parametrisation, the topology optimisation problem can be interpreted as finding the optimal material density distribution over a given design domain leading to cost minimisation. Hence, we define our optimisation problem as follows:

$$\min_{\boldsymbol{\rho}}: \text{cost}(\boldsymbol{\rho}^{\text{phys}}, \mathbf{U}) \quad \text{or} \quad \text{cost}_{\text{alt},i}(\boldsymbol{\rho}^{\text{phys}}, \mathbf{U}), \quad (i = 1 \dots 3), \quad (22a)$$

$$\text{s.t.} : \begin{cases} \mathbf{K}\mathbf{U} = \mathbf{F}, \\ \frac{1}{n_e} \sum_{e=1}^{n_e} \rho_e^{\text{phys}} = V_m, \\ 0 \leq \boldsymbol{\rho} \leq 1. \end{cases} \quad (22b)$$

The problem at hand is a constrained optimisation problem, where the constraints are expressed in Eq. (22b). The first equality constraint is the state (i.e. equilibrium) equation (here for linear elasticity), with $\mathbf{K} \in \mathbb{R}^{|\mathcal{D}| \times |\mathcal{D}|}$ as the global stiffness matrix and $\mathbf{F} \in \mathbb{R}^{|\mathcal{D}|}$ as the global external force vector (zero in displacement control). The second equality constraint fixes the average of the total amount of material (used in the topology design) to be equal to the material volume fraction V_m . This volume constraint is well-known for stabilising the optimisation process and facilitating numerical convergence (Sigmund and Maute, 2013). The last constraint is an inequality (or a bound) constraint which allows for the smooth variation of the design variables only in the range between 0 and 1.

In each iteration of the optimisation process, the nodal displacements \mathbf{U} are first solved for from the equilibrium equation through FE analysis with the global stiffness matrix

$$\mathbf{K}(\boldsymbol{\rho}^{\text{phys}}, \boldsymbol{\theta}) = \bigcup_{e=1}^{n_e} \tilde{\rho}_e^{\text{phys}}(\rho_e^{\text{phys}}) \mathbf{K}_e(\boldsymbol{\theta}), \quad (23)$$

where the density assigned to each element directly influences the significance of the contribution of that element stiffness $\mathbf{K}_e(\boldsymbol{\theta}) \in \mathbb{R}^{|\mathcal{D}_e| \times |\mathcal{D}_e|}$ to the global stiffness of the domain. The stiffness matrix depends on the material parameters $\boldsymbol{\theta}$ which are the unknowns of the identification problem. Later in Section 4 we discuss how the choice of these parameters affects the optimised topologies. The modified physical density in Eq. (23) is given by

$$\tilde{\rho}_e^{\text{phys}} = \rho_{\min} + \left(\rho_e^{\text{phys}}\right)^3 (1 - \rho_{\min}) . \quad (24)$$

It is used to avoid singularity in the global stiffness matrix when $\rho_e^{\text{phys}} = 0$, by adopting a threshold value ρ_{\min} (here set to 10^{-9}). Moreover, the power of 3 is considered as a “magic” number which helps drive the grey scales towards 0 or 1 and maintain numerical convergence (Sigmund and Maute, 2013). This number has been confirmed to ensure the physical realisability of intermediate densities (Bendsøe and Sigmund, 1999), with which Amstutz (2011) verified the equality of density gradients and topological derivatives for elasticity. Regarding the discretisation, we employ bilinear quadrilateral elements with 4 Gauss points under plane-stress conditions, maintain equal size for all elements, and keep a fixed uniform mesh throughout the optimisation process. Topology optimisation without regularisation is an ill-posed problem which can lead to checkerboard patterns (Andreassen et al., 2011). For this reason, *filtering* techniques have been developed. Filtering serves as a regularisation scheme, transforming the sharp, binary, 0-1 topology (represented by $\boldsymbol{\rho}$) to a smeared, grey-scale topology (represented by $\boldsymbol{\rho}^{\text{avg}}$) and is necessary to achieve convergence to a local minimum. In Appendix C we summarise explicit and implicit filtering approaches to transform $\boldsymbol{\rho}$ to $\boldsymbol{\rho}^{\text{avg}}$. Therein, we justify our choice of an implicit PDE filter defined in Eq. (C.6). The grey scale densities $\boldsymbol{\rho}^{\text{avg}}$ are undesirable in the output topology since they cannot be manufactured in practice. To convert $\boldsymbol{\rho}^{\text{avg}}$ into a black-and-white topology represented by $\boldsymbol{\rho}^{\text{phys}}$, we employ *projection* filtering, see Eq. (C.7). To achieve a desired transition to the black-and-white design, Appendix C also discusses a gradual increase of the projection filter strength parameter ψ over 10 optimisation loops.

Recalling Eq. (22a), we notice that the cost function is defined in terms of the physical (i.e., projected) densities $\boldsymbol{\rho}^{\text{phys}}$, which depend through the projection filter in Eq. (C.7) on the weight-averaged densities $\boldsymbol{\rho}^{\text{avg}}$, with these depending on the design variables $\boldsymbol{\rho}$ through the PDE filter in Eq. (C.6). Consequently, the following chain rule must be applied while computing the gradients (see Appendix D):

$$\frac{d(\text{cost})}{d\boldsymbol{\rho}} = \frac{d(\text{cost})}{d\boldsymbol{\rho}^{\text{phys}}} \frac{d\boldsymbol{\rho}^{\text{phys}}}{d\boldsymbol{\rho}^{\text{avg}}} \frac{d\boldsymbol{\rho}^{\text{avg}}}{d\boldsymbol{\rho}} . \quad (25)$$

With the construction above and the definition in Eq. (21), the cost is a non-convex and non-linear function of the design variables $\boldsymbol{\rho}$. This implies the existence of multiple local minima for the optimisation problem, highlighting the influence of the initial guess for domain initialisation. We investigate this influence in Appendix E.

3.4. Robust topology optimisation to ensure a minimum length scale

Weight-averaged density filtering introduces a minimum length scale by means of regularisation. Projection filtering has the opposite effect and often leads to the formation of tiny material/void regions (Sigmund, 2009). The existence of a minimum length scale, a property referred to as *local* mesh convergence in the jargon of topology optimisation, prevents the formation of impractically small topological features which are susceptible to premature failure upon mechanical tests.

A promising method to ensure local convergence is the so-called *robust* formulation of topology optimisation (Sigmund, 2009; Wang et al., 2011). Based on this method, three sets of projected densities, denoted as eroded $\boldsymbol{\rho}_{(-)}^{\text{phys}}$, intermediate $\boldsymbol{\rho}^{\text{phys}}$, and dilated $\boldsymbol{\rho}_{(+)}^{\text{phys}}$ physical densities, generated by applying projection filtering through Eq. (C.7) with thresholds $\phi_{(-)}$, ϕ , and $\phi_{(+)} = 1 - \phi_{(-)}$, are employed in a robust cost function. The difference between the three designs generated by three different thresholds defines manufacturing error bounds on both solid and void phases in the optimised topology. The robust optimisation problem including the contribution of all three sets of projected

densities is defined as follows (Wang et al., 2011):

$$\min_{\rho} : \max \left(\text{cost}(\rho_{(-)}^{\text{phys}}, \mathbf{U}_{(-)}), \text{cost}(\rho^{\text{phys}}, \mathbf{U}), \text{cost}(\rho_{(+)}^{\text{phys}}, \mathbf{U}_{(+)}) \right), \quad (26a)$$

$$s.t. : \begin{cases} \mathbf{K}_{(-)} \mathbf{U}_{(-)} = \mathbf{F}, \\ \mathbf{K} \mathbf{U} = \mathbf{F}, \\ \mathbf{K}_{(+)} \mathbf{U}_{(+)} = \mathbf{F}, \\ \frac{1}{n_e} \sum_{e=1}^{n_e} \rho_{e,(+)}^{\text{phys}} = V_m \frac{V_{(+)}}{V}, \\ 0 \leq \rho \leq 1, \end{cases} \quad (26b)$$

where the displacements $\mathbf{U}_{(-)}$, \mathbf{U} and $\mathbf{U}_{(+)}$ are obtained by performing three separate FE analyses with respective global stiffness matrices $\mathbf{K}_{(-)}$, \mathbf{K} and $\mathbf{K}_{(+)}$ for the three sets of physical densities. The volume constraint in Eq. (26b) is applied to the dilated physical densities; this is introduced in Wang et al. (2011) to eliminate the numerical artefacts observed in Sigmund (2009) due to using intermediate densities directly. On the right-hand side of the volume constraint, the material volume fraction V_m is multiplied by the ratio of the dilated-to-intermediate volume fractions such that the intermediate densities still follow V_m . At the end of the optimisation process, the intermediate physical densities ρ^{phys} represent the robustly optimised topology. Here, we use $\phi_{(-)} = 0.25$, $\phi = 0.50$ and $\phi_{(+)} = 0.75$. Note that the minimum length scale introduced by the robust approach increases as $|\phi - \phi_{(-)}|$ grows. Also, the radius of weight-averaged density filtering directly influences the minimum length scale, see Wang et al. (2011) for details.

3.5. Optimisation algorithm

The optimisation algorithm is responsible for updating the design densities in a way that leads to cost minimisation while satisfying the constraints. Having a number of design variables in the order of 10^5 , we choose a gradient-based optimisation strategy and employ MATLAB's general-purpose, gradient-based, constrained optimiser *fmincon* with its *interior-point* method. This method solves a sequence of approximate minimisation problems constructed by adding up the original cost with weighted logarithmic barrier functions, each dependent on a slack variable, with as many slack variables as inequality constraints. The slack variables are adopted to transform the inequality constraints into equality constraints. Meanwhile, the slack variables are restricted to be positive to keep the iterates in the *interior* of the feasible region. As the weighting factor of the barrier functions decreases to zero, the minimum of the approximate problem approaches the minimum of the original cost function. The equality constraints are incorporated with the help of Lagrange multipliers. The approximate problem is then solved using either a direct Newton step or a conjugate gradient step using a trust region method. The default is the former, and if it fails (e.g. due to non-convexity near the current iterate), the algorithm resorts to the latter, see The MathWorks Inc. (2024a) for further details. We provide as inputs first-order analytical derivatives (i.e., sensitivities) of the cost with respect to the design variables, which we derive via the adjoint method in Appendix D. The second-order derivatives of the cost function are approximated by *fmincon* via the LBFGS approach (The MathWorks Inc., 2024a).

To begin the optimisation process, we need an initialisation guess for the design densities ρ that satisfies the volume constraint applied on ρ^{phys} . Fig. 2b shows the initialisation setup with evenly distributed densities, commonly used as a starting guess in topology optimisation and adopted here as the default choice. Figures 2c and 2d show alternative initialisations, which are employed as initial guesses in Appendix E. Furthermore, the stopping criterion in control of the termination of the optimisation loop comprises two conditions: the maximum relative change in the design densities falling below 10^{-4} , and the maximum number of iterations exceeding 50. Whichever of these two conditions is met, the optimisation loop terminates. In our experience, these conditions allow the topology to evolve gradually without many idle iterations.

Fig. 3 presents the flowchart of the optimisation algorithm. As per this flowchart, to start the optimisation algorithm, the material volume fraction V_m , initial design densities ρ , the filtering radius r_{\min} , the initial projection filter strength $\psi = 1$, and the material parameters θ must be defined. Then, the filtering operation takes place, providing us with the actual topology made by ρ^{phys} . Next, the FE analysis is performed to find the displacement and strain fields which are handed over to the routine which performs the cost and sensitivity computation. The optimiser engine then recruits this information to update the design densities in the direction of the cost minimisation while respecting the constraints. The algorithm keeps iterating until meeting the stopping criterion, thereby doubling the filter parameter

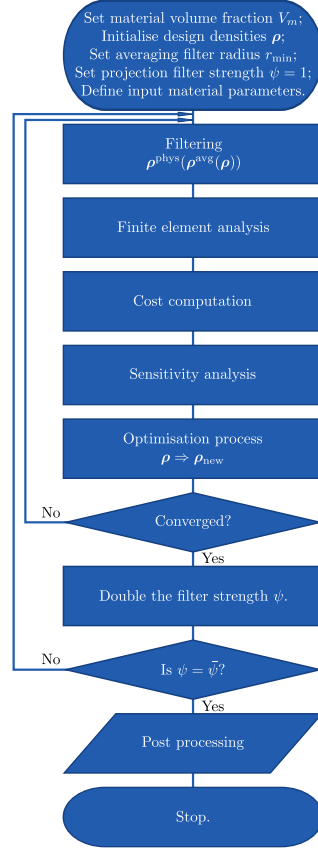


Figure 3: Flowchart of the overall optimisation algorithm with gradual increase of the strength of the projection filter (adapted from [Bendsøe and Sigmund \(2004\)](#)).

ψ to help binarify the topology, and hence continuing until $\psi = \bar{\psi}$ to approach a black-and-white design. Eventually, in case of the presence of minor grey scales in the optimised topology, a post-processing, hard-thresholding step is performed which outputs a sharp 0-1 design.

4. Results and discussion

In this section, we present the main results of our topology optimisation framework to design optimal specimens for noise-tolerant identification of constitutive parameters in isotropic and anisotropic linear elasticity. Further results are reported in the Appendices.

4.1. Optimisation process and global (mesh) convergence for isotropic elasticity

This section examines the performance of the cost functions in Eq. (20) (with $p = 8$) and Eq. (21) by analysing their optimisation process, the strain fields in their output topology subjected to the tensile test of Fig. 2, and their mesh convergence behaviour. The results from the cost functions in Eq. (20) and Eq. (21) are given in Fig. 4 and Fig. 5, respectively. An isotropic material with Young's modulus $E = 200$ GPa and Poisson's ratio $\nu = 0.3$ is assumed for this analysis.

Figs. 4a and 5a illustrate the topology optimisation process. Each plot shows the evolution of the cost (red diamonds) and topology against the number of iterations during optimisation. Each optimisation process is initialised with evenly distributed densities (as shown earlier in Fig. 2b), and a cost of one due to the normalised definition. In the next iteration, the weight-averaging PDE filter becomes active, which induces some blur in the topologies and a sharp jump in the cost value. Shortly after, there is a rapid drop in the cost until iteration #7 in Fig. 4a and iteration #4

in Fig. 5a, where an early-stage picture of the topology emerges. At iteration #51, the algorithm reaches the maximum number of iterations per optimisation loop and the projection-filter parameter ψ is doubled, which stimulates stronger 0-1 binarification as well as a sharp drop in the cost value. The algorithm continues similarly with the next optimisation loops, gradually leading to a black-and-white topology. Overall, both cost functions exhibit mostly decreasing values during the course of optimisation (except for a few iterations). After four loops in Fig. 4a and seven loops in Fig. 5a, each consisting of 50 iterations, the changes in the topologies become rather negligible, thereby activating the other stopping criterion, i.e., the lower bound on the maximum relative change in the design densities, resulting in a more rapid termination of the remaining loops. The final optimised topologies are delivered at the end of loop #10 (when $\psi = \bar{\psi}$). To speed up the optimisation process, a possibility could be setting the stopping criteria adaptively to allow less strict termination of the algorithm in the last 4-5 optimisation loops, as they are mainly responsible for increasing the contrast of the design, i.e., binarification. However, to ensure a smooth and gradual topology update, we have not incorporated such adaptive stopping criteria. To quantify the discreteness of the optimised topologies, Sigmund (2007) define a grey-level index as

$$g_{\text{idx}} = \frac{4}{n_e} \sum_{e=1}^{n_e} \rho_e^{\text{phys}} (1 - \rho_e^{\text{phys}}). \quad (27)$$

Designs with $g_{\text{idx}} < 1\%$ are recognised as sufficiently discrete. Using this metric, our optimised topologies in Fig. 4a and Fig. 5a yield $g_{\text{idx}} = 0.39\%$ and 0.20% , respectively. The optimised designs finally undergo post-processing with hard thresholding to ensure $g_{\text{idx}} = 0$ in the final output. The comparison among the two cost functions shows a steadier behaviour (i.e., declining more uniformly through longer-lasting optimisation loops) as well as a smaller final grey-level index for the cost function in Eq. (21). Both optimised topologies contain two symmetric holes in the top and bottom halves of the specimen, and the one reached by the cost function in Eq. (20) contains two more holes. The 2-norm condition number is similar for both designs; it is given by $\kappa_2 = 193$ and 204 for the topologies in Fig. 4a and Fig. 5a, respectively.

Figs. 4b and 5b plot the contours of the strain components ε_{11} , ε_{22} and γ_{12} . For the loading conditions in Fig. 2b, ε_{11} is almost zero in both specimens, whereas ε_{22} shows concentrations and gradients at the side corners of the holes and at the four outer corners. Similarly, the shear strain also exhibits some concentrations. The ranges of strain values for the two specimens are almost identical. However, the two additional side holes in Fig. 4b generate some minor gradients of the shear strain component, a favourable feature missing in Fig. 5b. In the next section we provide quantitative measures to highlight the importance of the strain patterns generated as a result of topology optimisation.

Figs. 4c and 5c investigate the *global* convergence of the optimised topologies as the total number of DOFs (nDOFs) increases. The determinant-based cost function leads to acceptable mesh convergence, with only minor changes as the FE grid is refined. The slight distortion of the holes at nDOFs $\approx 10^6$ is likely due to the effect of roundoff error. The mesh refinement level with nDOFs $\approx 10^{5.5} \approx 3.2 \times 10^5$ (yielding $n_e \approx 1.6 \times 10^5$ design variables) is considered sufficient for convergence, and all further analyses are based on it. Conversely, $\kappa_p(\mathbf{A}^{\text{eqb}})$ renders an inferior convergence behaviour since the optimised topologies continue to change while the FE mesh is refined. We note that the consistent definition of the weighting parameters λ_r and λ_q (as discussed in Appendix A) is of crucial importance to achieve global convergence in the optimised topologies. Considering all the aspects discussed above, the determinant-based cost function from Eq. (21) proves to be the best choice. This statement continues to hold also for anisotropic materials, as exemplified later. Therefore, from now on we only focus on the determinant-based cost function in Eq. (21). In Appendix B we provide more results for the cost function in Eq. (20) and explore a few additional cost definitions.

4.2. Topology optimisation for material parameter identification in orthotropic elasticity

As mentioned in Sections 3.2 and 3.5, the topology optimisation framework requires the material parameters as inputs to be able to solve for the nodal displacements through the FE analysis in Eq. (22b). This may sound problematic, as the material parameters are the unknowns of the parameter identification for which the specimen is to be designed. In this section, we aim to investigate the effect of the input material parameters on the output topologies. To this end, we focus our attention on orthotropic materials under the plane stress assumption. Such materials exhibit different stiffness properties along two orthogonal in-plane directions (material local coordinates), as shown in Fig. 1. We denote with x the strong material direction, situated at an angle β from the global coordinate 1, and with y the

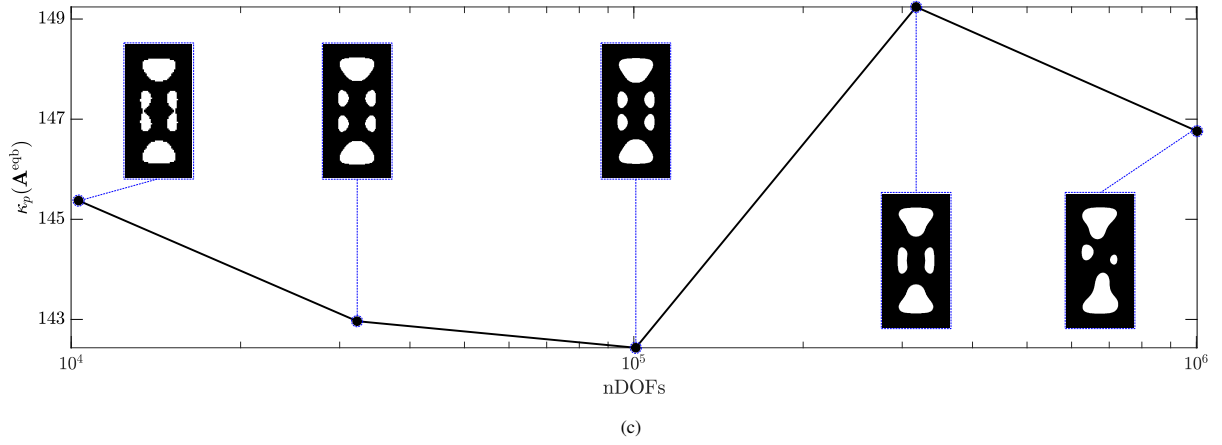
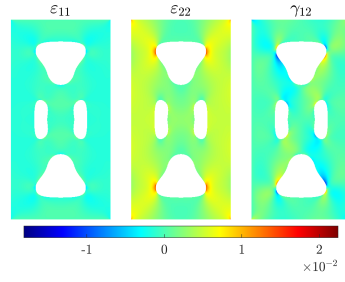
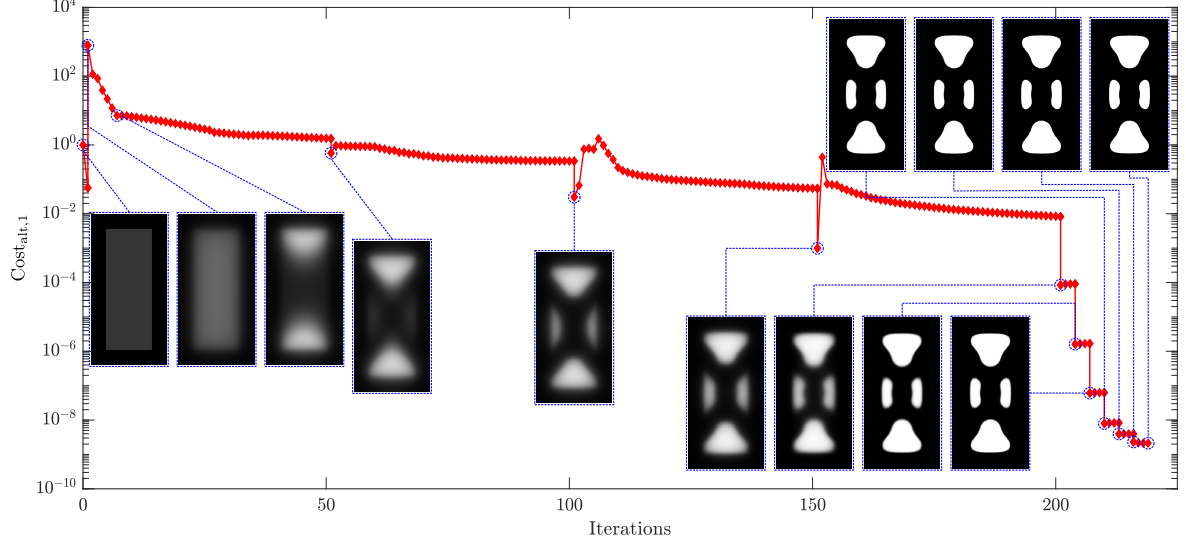
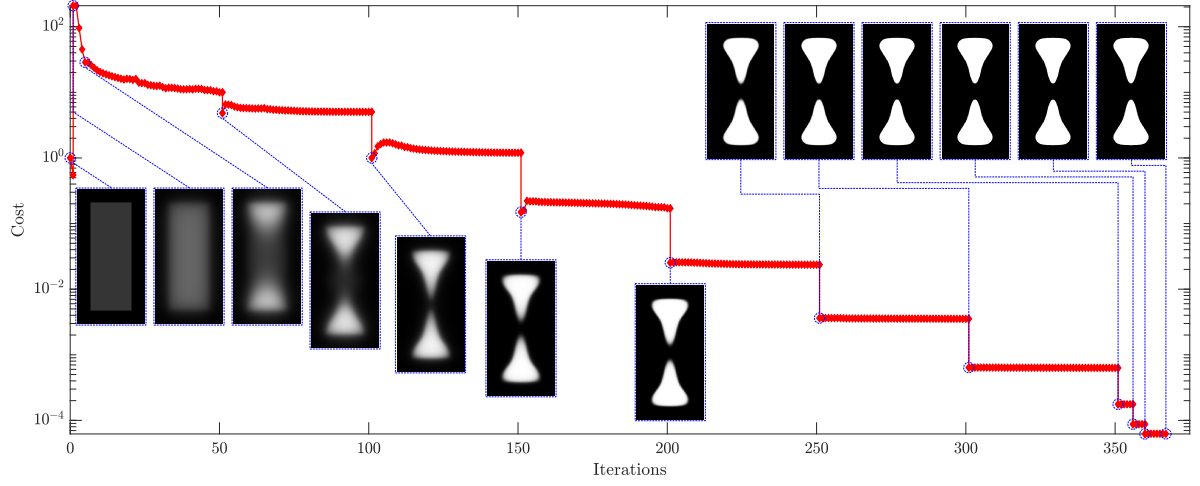
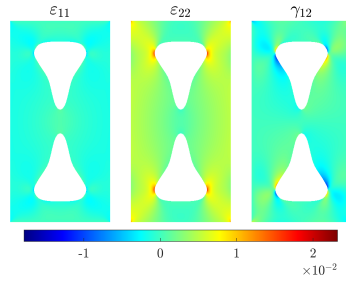


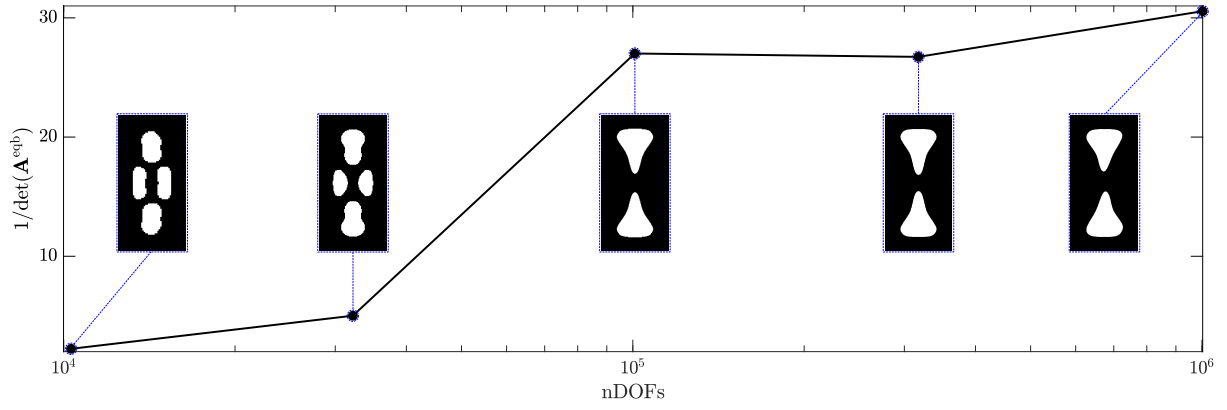
Figure 4: (a) Evolution of the cost function in Eq. (20) and of the topology during optimisation; (b) contours of the strain components for the optimised topology; (c) final cost and optimised topology versus mesh refinement.



(a)



(b)



(c)

Figure 5: (a) Evolution of the cost function in Eq. (21) and of the topology during optimisation; (b) contours of the strain components for the optimised topology; (c) final cost and optimised topology versus mesh refinement.

weak material direction. To characterise the planar behaviour of orthotropic materials, four parameters are required: the longitudinal Young's modulus, E_{xx} , the transverse Young's modulus E_{yy} , the in-plane shear modulus G_{xy} , and the in-plane Poisson's ratio ν_{xy} (or the transverse Poisson's ratio $\nu_{yx} = \nu_{xy} E_{yy}/E_{xx}$). To characterise the intensity of anisotropy, we utilise the two dimensionless parameters introduced in [Nejati et al. \(2019\)](#):

$$\alpha_1 = \frac{E_{xx}}{E_{yy}} \quad \alpha_2 = \frac{G_{xy}}{G_{xy}^{sv}}, \quad (28)$$

with

$$\frac{1}{G_{xy}^{sv}} = \frac{1}{E_{xx}} + \frac{1}{E_{yy}} + \frac{2\nu_{xy}}{E_{xx}}. \quad (29)$$

Note that for an isotropic material $\alpha_1 = \alpha_2 = 1$. Based on the analysis in [Nejati et al. \(2019\)](#), the constitutive response is predominantly governed by the anisotropy ratios α_1 , α_2 and the anisotropy angle β , whereas the influence of ν_{xy} is negligible. Thus, we consider the range of material parameters in Table 1, representing a broad spectrum of orthotropic materials, to be given as inputs to the topology optimisation framework. Due to the normalisation of the cost function, we expect only these dimensionless ratios to affect the results.

Table 1: Material properties to define a range of orthotropic materials.

| α_1 | α_2 | β ($^\circ$) | ν_{xy} |
|-----------------------|-----------------------------|------------------------|------------|
| $\{4, 8, \dots, 20\}$ | $\{0.5, 0.75, \dots, 1.5\}$ | $\{0, 15, \dots, 90\}$ | 0.3 |

Fig. 6 portrays the topologies generated using in input some of the orthotropic material parameters from Table 1 and a material volume fraction of $V_m = 80\%$. The first observation is that the choice of the input material affects the optimised topology, with the most significant changes resulting from the variation of the anisotropy angle β . We later use this information to quantify the performance of selected topologies. Comparing Fig. 6 with Fig. 5 for the isotropic case, we note that similar holes form when the strong material direction coincides with the loading axis ($\beta = 90^\circ$). As the anisotropy angle decreases towards 0° , the holes tend to deform accordingly. Along with this deformation, the holes may merge or decompose into smaller pieces. These changes result from a complex interplay between the anisotropy orientation and the ensuing strain field (which determines $\det(\mathbf{A}^{\text{eqb}})$), the weight-average filtering, the presence of the outer passive frame, and the constraint of fixed material volume fraction. Another prominent feature in the optimised topologies is their (bisect-dual-flip) symmetry, which is a consequence of symmetry in \mathbf{A}^{eqb} , symmetric loading configuration, and evenly distributed initialisation densities. It is shown in [Appendix E](#) that initialisations with sufficient randomness can disrupt such symmetric patterns. Lastly, we observe that a few topologies contain narrow strips of material connecting the holes, which may prematurely fail upon loading the specimen in a real experiment. In Section 4.3 we discuss the application of robust topology optimisation as a remedy to this issue.

We now assess the performance of the optimised specimen topologies for identification of the material parameters θ . Note that θ contains $n_f = 6$ unknown stiffness components as in Eq. (5), since the material is assumed to be linearly elastic with no information on the type of material symmetry. We use artificially generated deformation fields, perturb the strains at the integration points with Gaussian noise with zero mean and standard deviation $\gamma_f = 10^{-3} \times \bar{u}/L_Y$, where \bar{u}/L_Y is the nominal strain applied to the specimen, and perform no denoising. We apply the already created topologies to identify the elastic material properties which can be generated via the inputs in Table 1. We select as representative the seven topologies generated by $(\alpha_1, \alpha_2) = (12, 1.0)$ from Fig. 6, and investigate their effectiveness for parameter identification. Further, to provide some insight on the effect of the material volume fraction, we generate the respective set of topologies with $V_m = 70\%$ and $V_m = 90\%$. Fig. 7 illustrates the results, in terms of cost (without normalisation) and parameter identification error $\|\theta - \theta_{\text{gt}}\|_2 / \|\theta_{\text{gt}}\|_2$, where θ_{gt} is the vector of the ground-truth material parameters.

The most prominent trend observed in Fig. 7 is the overall decrease of both the cost and the identification error when the anisotropy angle varies from $\beta = 0^\circ$ to 90° under uniaxial loading, i.e. as the strong material direction comes closer to the loading direction, leading to a better identification of E_{xx} (since E_{xx} is the largest stiffness component, its identification error affects the ℓ_2 -norm error the most significantly). Furthermore, investigation of the individual identification error in each of the stiffness components reveals that, normally, the hardest parameter to be identified for

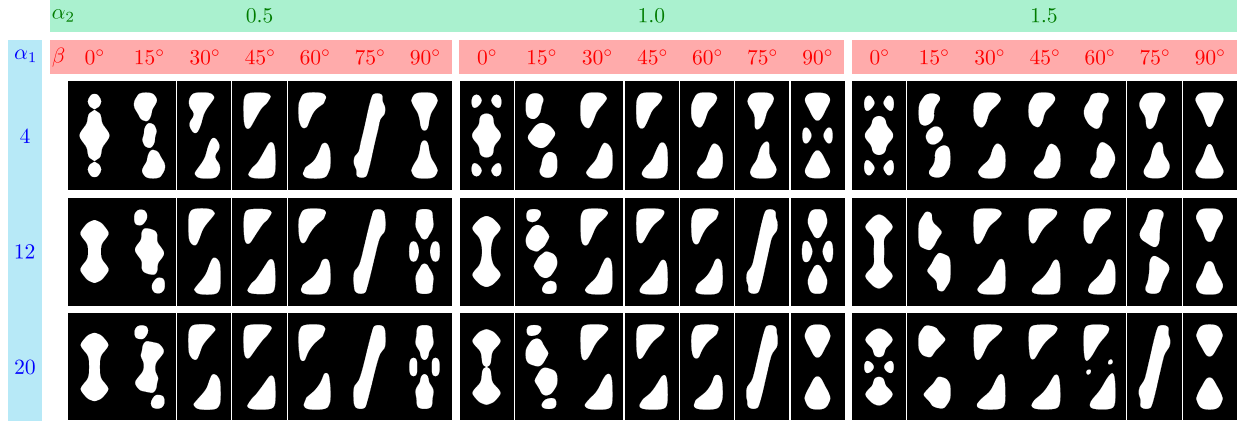


Figure 6: Optimised topologies for different orthotropic material parameters in input. The densities are initialised evenly, and the material volume fraction is set to $V_m = 80\%$.

$\beta < 45^\circ$ is E_{xx} , for $\beta > 45^\circ$ is E_{yy} , and for $\beta = 45^\circ$ is G_{xy} . Considering the middle-row results pertaining to $V_m = 80\%$ in Fig. 7, we see that the different optimised topologies yield different costs, with the topologies optimised for $\beta = 15^\circ$ and 90° outperforming the rest in almost all cases. As an example, to calibrate the material parameters for orthotropic materials with $\beta = 0^\circ$, considering the medians in the boxes and whiskers as representative, the unnormalised cost for the 15° topology is $2.14 \times 10^3 \text{ mm}^{-12}$, while for the 0° topology it is $6.52 \times 10^3 \text{ mm}^{-12}$. As for the identification error, the 15° topology delivers the lowest error of 10%, while the 0° topology gives 13%. The better performance of the topologies optimised for $\beta = 15^\circ$ and 90° can be explained with the closely spaced holes appearing in these two specimens, which cause localised strain gradients adjacent to the holes. Considering the results for $V_m = 70\%$ and 90% , a similar superiority in performance is observed for the topologies created with $\beta = 15^\circ$ in the former, and with $\beta = 0, 15$ and 90° in the latter, again due to the effect of tightly arranged holes. Overall, it is unexpected that certain topologies be superior to others in almost all cases. We would rather expect that every topology produced for a material with a specific β be the optimal topology for identifying materials with that value of β . A possible justification is the non-convexity of the cost function and the effect of initialisation which can lead the optimisation to a local minimum, as illustrated in more detail in Appendix E. A further reason may be the projection filtering which induces abrupt changes in the optimised topologies as the input anisotropy angle varies between 0° and 90° . We shed more light on this in Section 4.3. Comparing the results for different material volume fractions in Fig. 7, it is evident that the optimised topologies remain quite consistent as V_m changes. With the increase of V_m , the holes may shrink and decompose into smaller holes, or coalesce and form fewer but larger holes. The lowest identification error bounds belong to $V_m = 90\%$. A possible explanation is that a higher material volume fraction enriches the system of equations in Eq. (14) with more material points. However, the limit case of $V_m = 100\%$ (not shown here) expectedly leads to exploding identification errors. The plot for $V_m = 90\%$ shows that the performance differences between the optimised topologies are rather small, hence the topologies optimised with different anisotropy angles perform (almost) equally well in the material identification process. This is an important point as it diminishes the significance of defining accurate material parameters as inputs to the topology optimisation framework. Here, by the definition of input material parameters, we simply mean defining the anisotropy ratios α_1, α_2 and the anisotropy orientation β , while the actual individual stiffness components gathered in θ are not required. Using the actual material parameters to design the test specimen contradicts the purpose of the constitutive law calibration, yet it has not been addressed in the literature (Chamoïn et al., 2020; Almeida et al., 2020; Barroqueiro et al., 2020; Gonçalves et al., 2023). Based on the above practically admissible results, we would recommend running the topology optimisation algorithm for a few anisotropy orientations (e.g. $\beta = 0, 15$ and 90°) with arbitrary α_1 and α_2 values, and then pick the specimen design with the largest number of holes, which is expected to enable robust identifiability for any 2D orthotropic material.

We provide a more explicit representation of the dependence of the cost function on the material volume fraction in Fig. 8. Here, we plot $1/\det(\mathbf{A}^{\text{eqb}})$ versus the material volume fraction in the range $V_m = 80 - 100\%$ for six simple topologies created manually and numbered according to the number of holes. The reason behind choosing simple

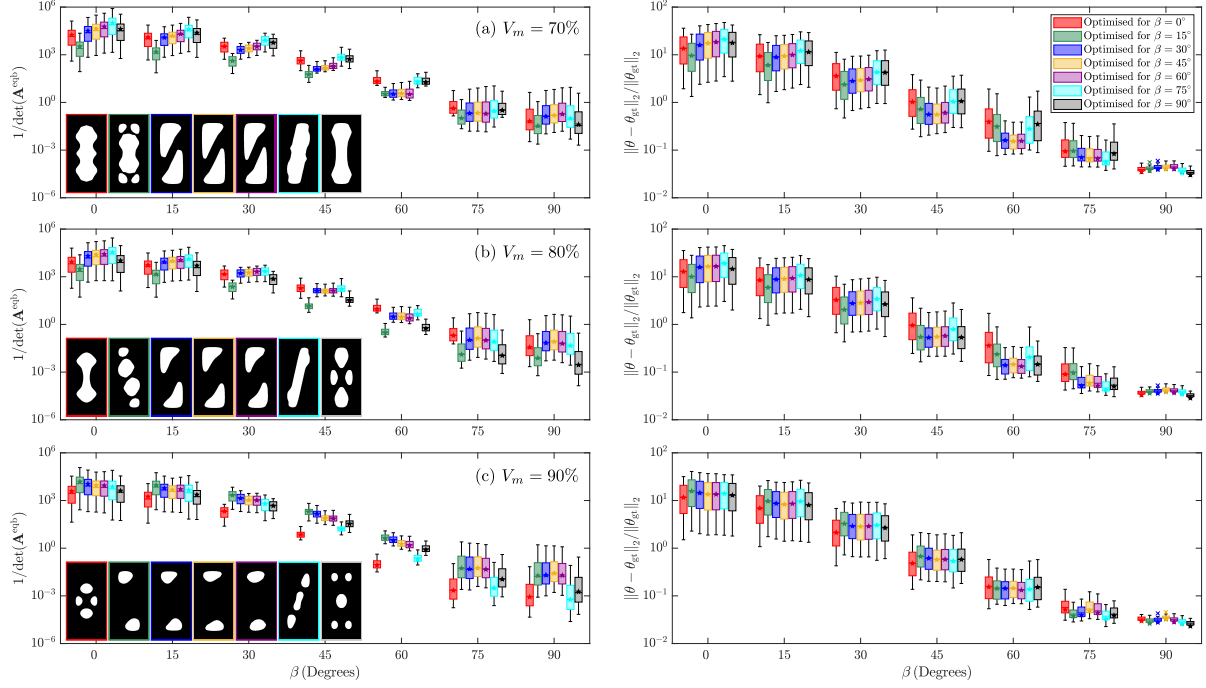


Figure 7: Identification of the orthotropic material parameters using optimised topologies obtained with $(\alpha_1, \alpha_2) = (12, 1.0)$ with different volume fractions. The left plots visualise the unnormalised cost (in mm^{-12}) while the right ones report the identification error (in percentage), both against the anisotropy angle β . The boxes and whiskers represent the range of results for different anisotropy ratios α_1 and α_2 . The cross signs (x) denote the outliers (i.e. cases lying $1.5 \times$ (interquartile range) away from the top or bottom of the boxes) and the star signs (★) designate the cases which have the same α_1 and α_2 value as the optimised topologies.

topologies is the ability to reproduce them exactly (to exclude the influence of shape change) with different volume fractions. It is not feasible to account for low volume fractions as they lead to invalid topologies, sometimes causing shape changes with merging holes, or introducing narrow strips of material (as also in the case of topology #6 at $V_m = 80\%$), which are practically avoided in topology optimisation through filtering. The material under study is orthotropic with $(\alpha_1, \alpha_2) = (12, 1.0)$, and the plots in Fig. 8 reflect the average results for different anisotropy angles $\beta \in \{0, 15, \dots, 90\}$. Material volume fractions of $85\% \leq V_m \leq 90\%$ are observed to be optimal irrespective of the topology used, probably because such volume fractions lead to sufficient richness of the system of equations due to many material points while preserving a heterogeneous design with non-uniform strain maps. Increasing the volume fraction further has a negative impact, whereby the extreme case of the full plate (i.e., $V_m = 100\%$) has a dramatically higher cost due to its uniform strain distribution, hence loss of identifiability. On the other hand, the reduction of the volume fraction depletes the information available on the deformation field, yielding less accurate material parameters.

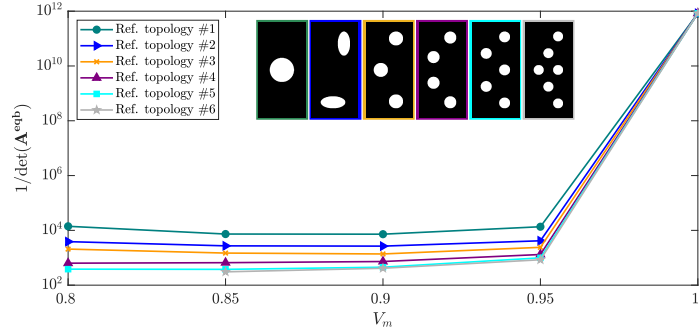
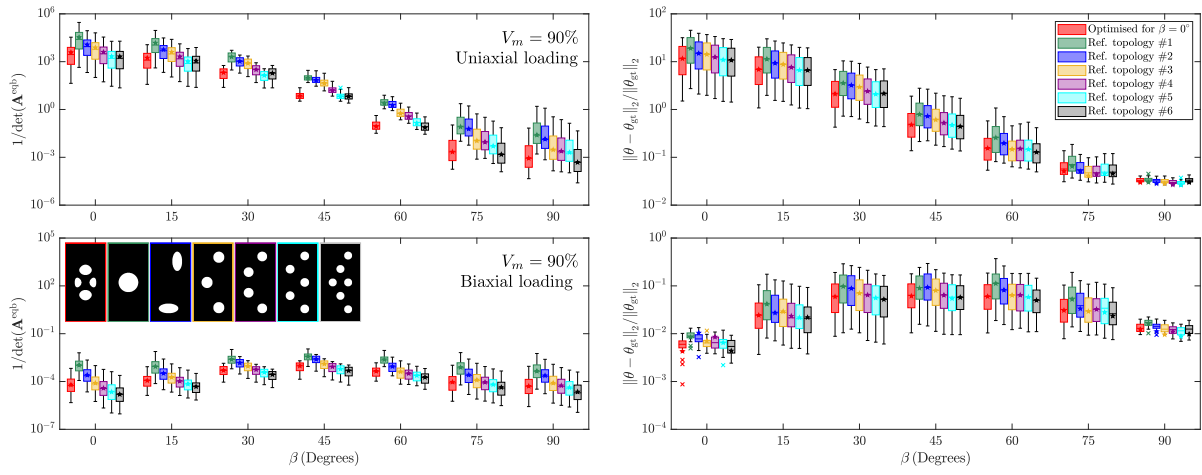
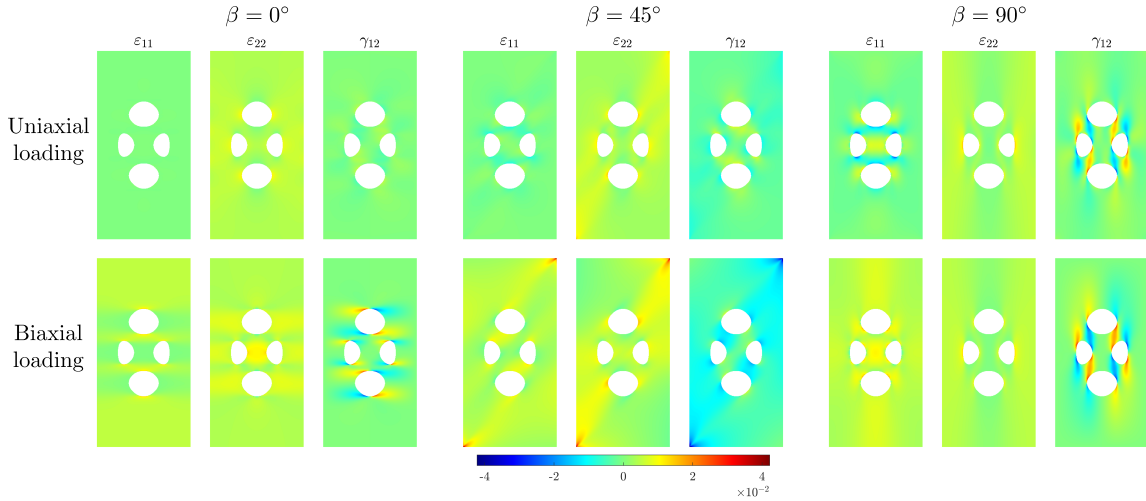


Figure 8: The dependence of the unnormalised cost (in mm^{-12}) on the material volume fraction investigated for six reference topologies.



(a)



(b)

Figure 9: Performance assessment of a chosen topology (produced with $(\alpha_1, \alpha_2, \beta) = (12, 1.0, 0^\circ)$ and $V_m = 90\%$ from Fig. 7) under uniaxial and biaxial tensile loading conditions: (a) comparison of the unnormalised cost (in mm^{-12}) and the identification error (in percentage) versus six reference topologies; (b) contours of strain components obtained for anisotropy orientations $\beta = 0, 45$ and 90° .

Fig. 9a compares the performance between the optimised topology generated with $(\alpha_1, \alpha_2, \beta) = (12, 1.0, 0^\circ)$ and

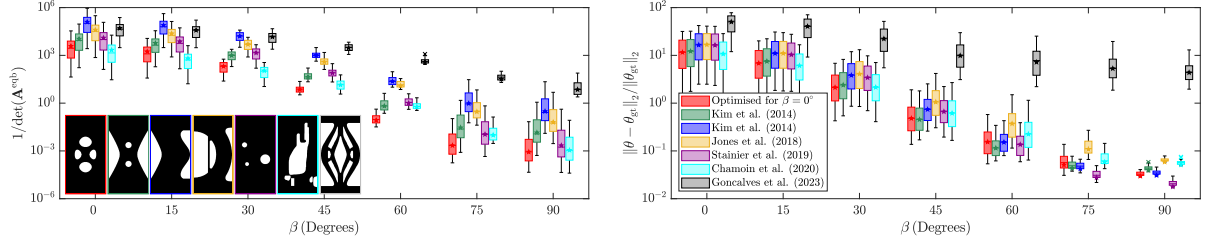


Figure 10: Performance assessment of a chosen topology (produced with $(\alpha_1, \alpha_2, \beta) = (12, 1.0, 0^\circ)$ and $V_m = 90\%$ from Fig. 7) versus selected designs from the literature under uniaxial tensile loading. The left plot visualises the unnormalised cost (in mm^{-12}) while the right one reports the identification error (in percentage), both against the anisotropy angle β .

the six reference topologies. All the topologies share the same material volume fraction $V_m = 90\%$. EUCLID has previously employed designs similar to reference topologies #1 and #2 to discover different classes of constitutive laws (Flaschel et al., 2021, 2022, 2023), although none of them concerned orthotropic materials. The remaining reference topologies should trigger more heterogeneous strain patterns as the number of their holes increases. The comparison is made for both uniaxial and biaxial loading (the latter applies an additional horizontal extension $u = \bar{u} \times L_X/L_Y$ to the right edge of the specimen). As shown in Fig. 9a and expected, the cost and the identification error decrease as the number of holes increases. However, results for topologies #5 and #6 are very similar, indicating that a saturation is reached, as also pointed out in Ihuaenyi et al. (2024). The selected optimised topology, which contains 4 but optimally designed holes, appears as effective as the most complex 6-hole manually designed topology, which is the advantage of the automated design via topology optimisation. Overall, the cost and identification error drop by orders of magnitude due to richer strain patterns in the biaxial loading setup (see Fig. 9b).

Fig. 9b illustrates the contours of the in-plane strain components for the automatically optimised topology, obtained by uniaxial and biaxial numerical experiments with $\beta = 0, 45$ and 90° . Under uniaxial loading, the case $\beta = 0^\circ$ results in rather uniform strain fields with negligible horizontal and shear strains. For $\beta = 45^\circ$, the strain contours acquire directional variations and larger values, and gradients of the shear strain appear. For $\beta = 90^\circ$, the largest values of the strains and their gradients are obtained. Changing the loading condition to biaxial further improves the results by generating more heterogeneous strain patterns also for $\beta < 45^\circ$. This may explain the discussed trends of cost and identification error observed in Figs. 7 and 9a when β changes from 0° to 90° .

Upon a request by the reviewers, in Fig. 10 we compare the performance of our optimised topology (generated with $(\alpha_1, \alpha_2, \beta) = (12, 1.0, 0^\circ)$) against selected topologies designed in the literature (Kim et al., 2014; Jones et al., 2018b; Stainier et al., 2019; Chamoine et al., 2020; Goncalves et al., 2023). Such a comparison has to be considered with caution because of two main reasons: (1) each specimen from the literature has been designed for the identification of different and specific material models, from linear elasticity (Stainier et al., 2019; Chamoine et al., 2020), to elasto-plasticity (Kim et al., 2014; Goncalves et al., 2023) and visco-plasticity (Jones et al., 2018b), using different identification techniques; (2) each topology has a specific material volume fraction, size, aspect ratio, resolution, and loading configuration. While bearing in mind the limitations in (1), we have tried our best to address most of the discrepancies in (2) by redesigning the selected topologies with minimal changes (not expected to have considerable influences). This means that the redesigned specimens feature equal size, aspect ratio and resolution as well as loading configuration (i.e., uniaxial tensile loading with full-width grip at both ends), but have different material volume fractions. The comparison between the specimen designs is based on the identification of the linear elastic constitutive parameters produced via the inputs in Table 1 through the equilibrium gap method outlined in Section 2. The results in Fig. 10 reveal that our optimised topology performs very well in comparison to the literature designs, leading to lower costs and identification errors in a wide spectrum of the considered orthotropic materials. The notched 2-hole specimen by Kim et al. (2014) exhibits quite similar performance to our design, while the 3-hole specimen by Stainier et al. (2019) and the optimised specimen by Chamoine et al. (2020) are optimal in the very high and very low anisotropy orientation regimes, respectively. In contrast, the optimised specimen by Goncalves et al. (2023), probably due to its low volume fraction (as analysed in Figs. 7 and 8), leads to high identification errors.

4.3. Robust topology optimisation

In a few cases, the optimised topologies comprise narrow strips of material which are prone to premature failure upon testing. This issue mostly arises due to the application of the projection filter with a single threshold ϕ (to achieve a black-and-white design) since this destroys the minimum length scale introduced by weight-averaged density filtering (Wang et al., 2011). To solve this problem, we resort to the robust formulation to topology optimisation outlined in Section 3.4 to obtain a minimum length scale on the physical (i.e., projected) densities.

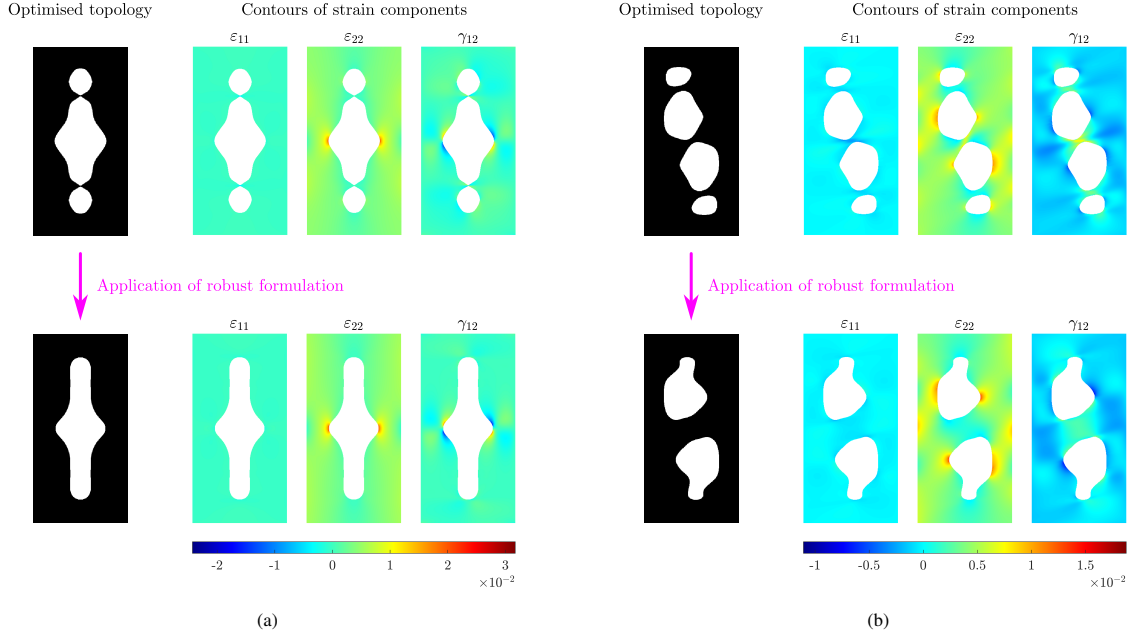


Figure 11: Effect of the *robust* formulation in topology optimisation to avoid tiny topological features: (a) topologies generated with inputs $(\alpha_1, \alpha_2, \beta) = (4, 0.5, 0^\circ)$; (b) topologies generated with inputs $(\alpha_1, \alpha_2, \beta) = (20, 1.0, 15^\circ)$.

Fig. 11 shows two sample cases from Fig. 6, produced with $(\alpha_1, \alpha_2, \beta) = (4, 0.5, 0^\circ)$ and $(20, 1.0, 15^\circ)$. The original topologies and their strain contours are shown in the upper row, where we note the existence of narrow strips of material and the consequent strain localisation which may lead to premature failure upon loading. Moreover, the DIC system fails to capture the deformation field in regions situated in the vicinity of the edges, resulting in the loss of valuable data. As shown in the lower row in Fig. 11, robust topology optimisation can fix the problem, leading to merged holes and wider material bands.

Fig. 12 presents the robustly optimised topologies and the performance of a few selected items in terms of cost and material identification error. Comparing the topologies in Fig. 12a with the ones in Fig. 6, it is clear that the robust formulation ensures local convergence, which also results in smoother changes of topologies as the anisotropy orientation β varies from 0° to 90° ; the generated holes tend to deform more consistently and more aligned with the anisotropy angle as opposed to the not robust topologies which transform more abruptly. We still observe narrow bands of solid material in the topology generated with the input $(\alpha_1, \alpha_2, \beta) = (4, 1.0, 15^\circ)$; in this case, the stopping criterion of maximum 50 iterations stops the first optimisation loop prematurely where more iterations are needed to reach convergence. Releasing this condition solves the problem.

Fig. 12b demonstrates the performance of selected optimised topologies generated by the robust formulation via inputs $(\alpha_1, \alpha_2) = (12, 1.0)$ from Fig. 12a. The overall performance trend for the robust topologies is similar to that of the not robust ones. However, as observed above, ensuring local convergence provides more consistency in the results as the anisotropy angle changes. This consistency can be noticed especially in the identification error plot, where the optimised topology for each anisotropy angle is almost always the best to identify the orthotropic material with that anisotropy angle.

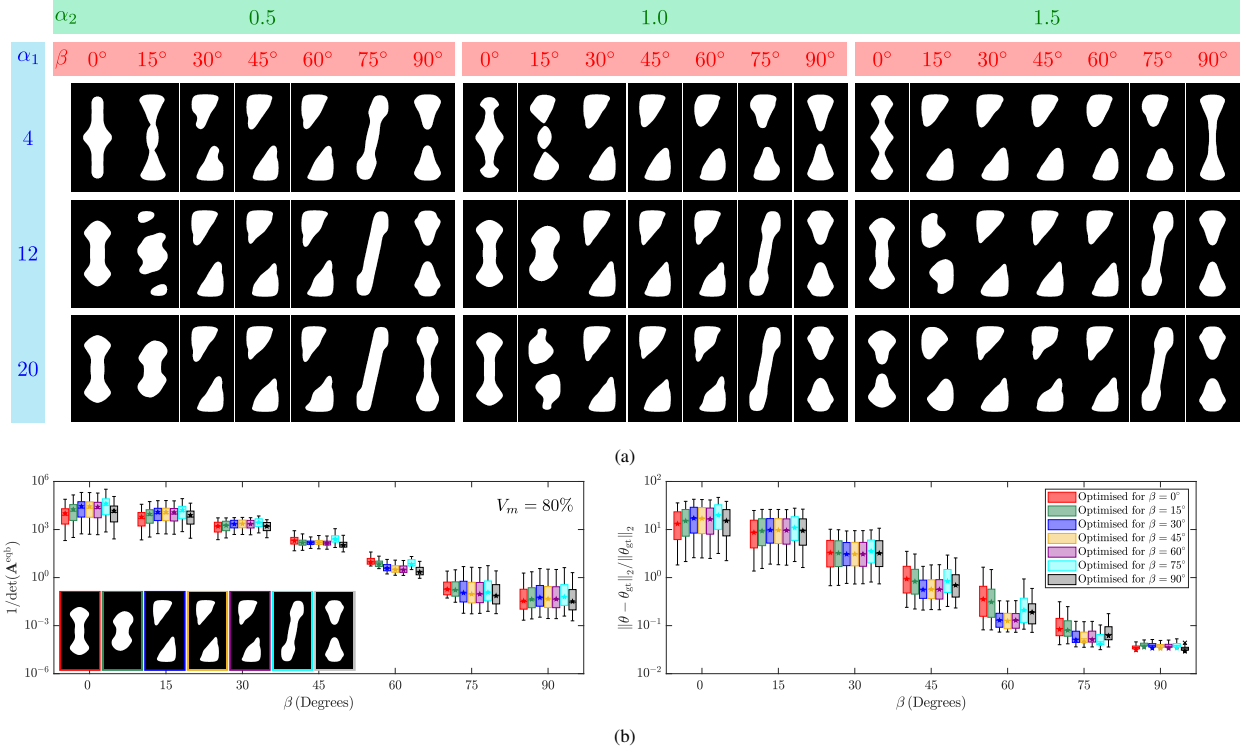


Figure 12: The application of the *robust* formulation in topology optimisation: (a) optimised topologies for different orthotropic materials. The densities are initialised evenly, and the material volume fraction is set to $V_m = 80\%$; (b) identification of the orthotropic material parameters using the optimised topologies obtained with $(\alpha_1, \alpha_2) = (12, 1.0)$ from part (a). The left plot visualises the unnormalised cost (in mm^{-12}) while the right one reports the identification error (in percentage), both against the anisotropy angle β .

5. Conclusions and outlook

We proposed a topology optimisation framework for the optimal design of the test specimen to be utilised for the one-shot identification or discovery of constitutive material models. To this end, we employed the density-based topology optimisation approach with a cost function targeting the robustness of the unknown material parameters against the noise in the experimental strain field. The developed framework was then used to generate optimised specimen designs to be tested in uniaxial or biaxial tensile experiments in order to calibrate isotropic as well as orthotropic material parameters in linear elasticity. The main findings can be summarised as follows:

- The equation system leading to the unknown material parameters involves a matrix \mathbf{A}^{eqb} which encodes all the information on the specimen geometry and boundary conditions. The conditioning of \mathbf{A}^{eqb} dictates the robustness of the identified material parameters against noise in the experimental strain data. In order to use a gradient-based optimisation technique, we propose as possible cost function a p -norm condition number or the inverse of the matrix determinant, which are continuously differentiable and independent of the ground-truth material parameters. The investigation of these and other cost functions reveals that $1/\det(\mathbf{A}^{\text{eqb}})$ behaves most stably, yields global mesh convergence, generates smoother topologies with fewer artefacts, and leads to the reduction of the identification error. Due to the non-convex nature of the cost function, the initial guess has a significant impact on the optimised topologies; a multi-start approach with various random initialisations potentially leads to the best design.
- The global convergence (i.e., mesh independence) of the optimised topologies is achieved through consistent definitions of the weighting factors λ_r and λ_q appearing in \mathbf{A}^{eqb} . Local convergence (i.e., ensuring the existence of a minimum length scale) in the optimised topologies is attained by implementing the robust formulation to topology optimisation, involving projection filtering with three different threshold values.

- For the efficient handling of a large number of design variables in topology optimisation, the sensitivities are calculated analytically via the adjoint method, which requires solving one additional FE-like problem. Moreover, the use of the PDE filter rather than the convolution-type operation reduces the memory consumption remarkably.
- The effect of input material parameters on the optimised topologies is investigated in the context of linear elastic orthotropic materials. Due to the normalised cost function, the anisotropy descriptors $\alpha_1 = E_{xx}/E_{yy}$, $\alpha_2 = G_{xy}/G_{xy}^{sv}$ and, most importantly, β (i.e., the anisotropy orientation) influence the optimised topologies whereas the individual values of the stiffness components are not relevant.
- The optimised topologies were evaluated in calibrating orthotropic material parameters. Due to the different relevance of the stiffness components under different anisotropy orientations β , the hardest parameter to calibrate in a uniaxial tensile test for $\beta < 45^\circ$ is E_{xx} , for $\beta > 45^\circ$ is E_{yy} , and for $\beta = 45^\circ$ is G_{xy} . The topologies optimised with different anisotropy orientations perform almost equally well, indicating a low influence of the input anisotropy orientation. Performance checks against reference topologies confirm the good performance of the optimised designs with few but optimally designed holes.

As future outlook, the performance of the optimised topologies in the calibration of constitutive parameters is to be experimentally evaluated. The current framework can be extended to more complex constitutive behaviours, e.g. hyperelasticity or dissipative behaviour. The further inclusion of DIC metrological features could lead to more practically optimised specimens.

Acknowledgement

SG and LDL acknowledge funding from the Swiss National Science Foundation through grant N. 200021_204316 “Unsupervised data-driven discovery of material laws”. Also, they thank Prof. Fabrice Pierron for fruitful discussion. SG thanks student Felix J. Lupp for his effort in improving the efficiency of the code.

Declaration of competing interest

The authors declare that they have no known competing financial interests or personal relationships that could have appeared to influence the work reported in this paper.

Code availability

The MATLAB code is publicly available at <https://gitlab.ethz.ch/compmech/euclid-top>.

References

- Acosta-Flores, M., Eraña-Díaz, M.L., 2024. Experimental determination of elastic properties in laminate composite material orthotropic plies. *Journal of Mechanical Science and Technology* 38, 1317–1328. doi:10.1007/s12206-024-0226-6.
- Almeida, F., Barroqueiro, B., Dias-de Oliveira, J., Andrade-Campos, A.G., 2020. On the Development of a Heterogeneous Mechanical Test Specimen Using Topology Optimization. *Procedia Manufacturing* 47, 816–823. doi:10.1016/j.promfg.2020.04.256.
- Amstutz, S., 2011. Connections between topological sensitivity analysis and material interpolation schemes in topology optimization. *Structural and Multidisciplinary Optimization* 43, 755–765. doi:10.1007/s00158-010-0607-6.
- Andreassen, E., Clausen, A., Schevenels, M., Lazarov, B.S., Sigmund, O., 2011. Efficient topology optimization in MATLAB using 88 lines of code. *Structural and Multidisciplinary Optimization* 43, 1–16. doi:10.1007/s00158-010-0594-7.
- Ascher, U.M., Greif, C., 2011. *A First Course in Numerical Methods*. Society for Industrial and Applied Mathematics, Philadelphia, PA. doi:10.1137/9780898719987.
- Barroqueiro, B., Andrade-Campos, A., Dias-de Oliveira, J., Valente, R., 2020. Design of mechanical heterogeneous specimens using topology optimization. *International Journal of Mechanical Sciences* 181, 105764. doi:10.1016/j.ijmecsci.2020.105764.
- Bendsøe, M.P., 1989. Optimal shape design as a material distribution problem. *Structural Optimization* 1, 193–202. doi:10.1007/BF01650949.
- Bendsøe, M.P., Sigmund, O., 1999. Material interpolation schemes in topology optimization. *Archive of Applied Mechanics (Ingenieur Archiv)* 69, 635–654. doi:10.1007/s004190050248.
- Bendsøe, M.P., Sigmund, O., 2004. *Topology Optimization*. Springer Berlin Heidelberg, Berlin, Heidelberg. doi:10.1007/978-3-662-05086-6.

- Bertin, M.B.R., Hild, F., Roux, S., 2016. Optimization of a Cruciform Specimen Geometry for the Identification of Constitutive Parameters Based Upon Full-Field Measurements. *Strain* 52, 307–323. doi:10.1111/str.12178.
- Bourdin, B., 2001. Filters in topology optimization. *International Journal for Numerical Methods in Engineering* 50, 2143–2158. doi:10.1002/nme.116.
- Bruns, T.E., Tortorelli, D.A., 2001. Topology optimization of non-linear elastic structures and compliant mechanisms. *Computer Methods in Applied Mechanics and Engineering* 190, 3443–3459. doi:10.1016/S0045-7825(00)00278-4.
- Chamoin, L., Jailin, C., Diaz, M., Quesada, L., 2020. Coupling between topology optimization and digital image correlation for the design of specimen dedicated to selected material parameters identification. *International Journal of Solids and Structures* 193–194, 270–286. doi:10.1016/j.ijsolstr.2020.02.032.
- Chapelier, M., Bouclier, R., Passieux, J.C., 2022. Spline-based specimen shape optimization for robust material model calibration. *Advanced Modeling and Simulation in Engineering Sciences* 9, 4. doi:10.1186/s40323-022-00217-9.
- Conde, M., Zhang, Y., Henriques, J., Coppieters, S., Andrade-Campos, A., 2023. Design and validation of a heterogeneous interior notched specimen for inverse material parameter identification. *Finite Elements in Analysis and Design* 214, 103866. doi:10.1016/j.finel.2022.103866.
- Flaschel, M., Kumar, S., De Lorenzis, L., 2021. Unsupervised discovery of interpretable hyperelastic constitutive laws. *Computer Methods in Applied Mechanics and Engineering* 381, 113852. doi:10.1016/j.cma.2021.113852, arXiv:2010.13496.
- Flaschel, M., Kumar, S., De Lorenzis, L., 2022. Discovering plasticity models without stress data. *npj Computational Materials* 8, 91. doi:10.1038/s41524-022-00752-4, arXiv:2202.04916.
- Flaschel, M., Kumar, S., De Lorenzis, L., 2023. Automated discovery of generalized standard material models with EUCLID. *Computer Methods in Applied Mechanics and Engineering* 405, 115867. doi:10.1016/j.cma.2022.115867, arXiv:2211.04453.
- Fu, J., Xie, W., Zhou, J., Qi, L., 2020. A method for the simultaneous identification of anisotropic yield and hardening constitutive parameters for sheet metal forming. *International Journal of Mechanical Sciences* 181, 105756. doi:10.1016/j.ijmecsci.2020.105756.
- Gonçalves, M., Andrade-Campos, A., Barroqueiro, B., 2023. On the design of mechanical heterogeneous specimens using multilevel topology optimization. *Advances in Engineering Software* 175, 103314. doi:10.1016/j.advengsoft.2022.103314.
- Grédiac, M., Pierron, F., 1998. A T-shaped specimen for the direct characterization of orthotropic materials. *International Journal for Numerical Methods in Engineering* 41, 293–309. doi:10.1002/(SICI)1097-0207(19980130)41:2<293::AID-NME284>3.0.CO;2-Y.
- Gu, X., Pierron, F., 2016. Full optimization of the T-shaped tensile test using genetic algorithm. Technical Report. University of Southampton. Southampton. URL: http://www.camfit.fr/documents/Progress_report_Xuesen_Tshape.pdf.
- Guélon, T., Toussaint, E., Le Cam, J.B., Promma, N., Grédiac, M., 2009. A new characterisation method for rubber. *Polymer Testing* 28, 715–723. doi:10.1016/j.polymertesting.2009.06.001.
- Guest, J.K., Prévost, J.H., Belytschko, T., 2004. Achieving minimum length scale in topology optimization using nodal design variables and projection functions. *International Journal for Numerical Methods in Engineering* 61, 238–254. doi:10.1002/nme.1064.
- Ihuenyi, R.C., Luo, J., Li, W., Zhu, J., 2024. Seeking the most informative design of test specimens for learning constitutive models. *Extreme Mechanics Letters* 69, 102169. doi:10.1016/j.eml.2024.102169.
- Johnson, S.G., 2012. Notes on adjoint methods for 18.335. URL: <https://math.mit.edu/~stevenj/18.336/adjoint.pdf>.
- Jones, E., Carroll, J., Karlson, K., Kramer, S., Lehoucq, R., Reu, P., Turner, D., 2018b. Parameter covariance and non-uniqueness in material model calibration using the Virtual Fields Method. *Computational Materials Science* 152, 268–290. doi:10.1016/j.commatsci.2018.05.037.
- Kim, J.H., Barlat, F., Pierron, F., Lee, M.G., 2014. Determination of Anisotropic Plastic Constitutive Parameters Using the Virtual Fields Method. *Experimental Mechanics* 54, 1189–1204. doi:10.1007/s11340-014-9879-x.
- Lazarov, B.S., Sigmund, O., 2011. Filters in topology optimization based on Helmholtz-type differential equations. *International Journal for Numerical Methods in Engineering* 86, 765–781. doi:10.1002/nme.3072.
- Nejati, M., Aminzadeh, A., Saar, M.O., Driesner, T., 2019. Modified semi-circular bend test to determine the fracture toughness of anisotropic rocks. *Engineering Fracture Mechanics* 213, 153–171. doi:10.1016/j.engfracmech.2019.03.008.
- Pierron, F., Grédiac, M., 2021. Towards Material Testing 2.0. A review of test design for identification of constitutive parameters from full-field measurements. *Strain* 57, 1–22. doi:10.1111/str.12370.
- Pierron, F., Vert, G., Burguete, R., Avril, S., Rotinat, R., Wisnom, M.R., 2007. Identification of the Orthotropic Elastic Stiffnesses of Composites with the Virtual Fields Method: Sensitivity Study and Experimental Validation. *Strain* 43, 250–259. doi:10.1111/j.1475-1305.2007.00346.x.
- Rojas-Labanda, S., Stolpe, M., 2015. Benchmarking optimization solvers for structural topology optimization. *Structural and Multidisciplinary Optimization* 52, 527–547. doi:10.1007/s00158-015-1250-z.
- Sigmund, O., 2007. Morphology-based black and white filters for topology optimization. *Structural and Multidisciplinary Optimization* 33, 401–424. doi:10.1007/s00158-006-0087-x.
- Sigmund, O., 2009. Manufacturing tolerant topology optimization. *Acta Mechanica Sinica* 25, 227–239. doi:10.1007/s10409-009-0240-z.
- Sigmund, O., Maute, K., 2013. Topology optimization approaches. *Structural and Multidisciplinary Optimization* 48, 1031–1055. doi:10.1007/s00158-013-0978-6.
- Souto, N., Andrade-Campos, A., Thuillier, S., 2016. A numerical methodology to design heterogeneous mechanical tests. *International Journal of Mechanical Sciences* 107, 264–276. doi:10.1016/j.ijmecsci.2016.01.021.
- Souto, N., Thuillier, S., Andrade-Campos, A., 2015. Design of an indicator to characterize and classify mechanical tests for sheet metals. *International Journal of Mechanical Sciences* 101–102, 252–271. doi:10.1016/j.ijmecsci.2015.07.026.
- Stainier, L., Leygue, A., Ortiz, M., 2019. Model-free data-driven methods in mechanics: material data identification and solvers. *Computational Mechanics* 64, 381–393. doi:10.1007/s00466-019-01731-1.
- Svanberg, K., 1987. The method of moving asymptotes—a new method for structural optimization. *International Journal for Numerical Methods in Engineering* 24, 359–373. doi:10.1002/nme.1620240207.
- The MathWorks Inc., 2024a. Constrained nonlinear optimization algorithms: fmincon interior point algorithm. URL: <https://ch.mathworks.com/help/optim/ug/constrained-nonlinear-optimization-algorithms.html#brnpd5f>.

- The MathWorks Inc., 2024b. Memoize: add memoization semantics to function handle. URL: <https://ch.mathworks.com/help/matlab/ref/memoize.html>.
- The MathWorks Inc., 2024c. Sparse: create sparse matrix. URL: <https://ch.mathworks.com/help/matlab/ref/sparse.html>.
- Tsai, S.W., 1965. Experimental Determination of the Elastic Behavior of Orthotropic Plates. *Journal of Engineering for Industry* 87, 315–317. doi:10.1115/1.3670829.
- Tung, C.h., Li, J., 2024. The anti-dogbone: Evaluating and designing optimal tensile specimens for deep learning of constitutive relations. *Extreme Mechanics Letters*, 102157doi:10.1016/j.eml.2024.102157.
- Wang, F., Lazarov, B.S., Sigmund, O., 2011. On projection methods, convergence and robust formulations in topology optimization. *Structural and Multidisciplinary Optimization* 43, 767–784. doi:10.1007/s00158-010-0602-y.
- Xu, S., Cai, Y., Cheng, G., 2010. Volume preserving nonlinear density filter based on heaviside functions. *Structural and Multidisciplinary Optimization* 41, 495–505. doi:10.1007/s00158-009-0452-7.
- Zhang, Y., Gothivarekar, S., Conde, M., de Velde, A.V., Paermentier, B., Andrade-Campos, A., Coppiters, S., 2022. Enhancing the information-richness of sheet metal specimens for inverse identification of plastic anisotropy through strain fields. *International Journal of Mechanical Sciences* 214, 106891. doi:10.1016/j.ijmecsci.2021.106891.

Appendix A. Consistent definition of the weighting parameters λ_r and λ_q

As introduced in Eq. (15a), there exist two weighting parameters λ_r and λ_q in the definition of \mathbf{A}^{eqb} . Here, we provide insight into the consistent definition of these parameters such that the cost functions defined in Eqs. (21) and (22) behave mesh convergent. Note that here we do not perform any topology optimisation, but rather look at a fixed sample geometry, i.e., the plate with one hole, as shown in Fig. 2a. The elastic anisotropic material considered here has 6 independent stiffness components gathered in $\boldsymbol{\theta} = [323, 100.03, 50.015, 190, 80.024, 144.930]^T$ GPa.

Fig. A.1a visualises, in logarithmic scale, the eigenvalues, the inverse of the determinant and the 2-norm condition number of \mathbf{A}^{eqb} against nDOFs as the FE mesh is refined. The eigenvalues, sorted in descending order, give n_f lines each with a slope m_i ($i = 1, \dots, n_f$). Hence, $1/\det(\mathbf{A}^{\text{eqb}})$ gives a line with the slope $-\sum_{i=1}^{n_f} m_i$, and $\kappa_2(\mathbf{A}^{\text{eqb}})$ gives a line with the slope $(m_1 - m_{n_f})$. In Fig. A.1a, $\lambda_r = \lambda_q = 1$, $m_1 \approx 0$ and m_i ($i = 2, \dots, n_f$) ≈ -0.5 . We aim at finding λ_r and λ_q such that all $m_i \approx 0$, thereby inducing mesh convergence in $1/\det(\mathbf{A}^{\text{eqb}})$ and $\kappa_2(\mathbf{A}^{\text{eqb}})$.

Let us first look at λ_r . This weighting parameter is required to balance the contributions of the free and fixed DOFs in the system of linear equations in Eq. (14) since $|\mathcal{D}^{\text{free}}|$ is usually significantly greater than $\sum_{s=1}^{n_s} |\mathcal{D}^{\text{fix},s}|$. To find the consistent value for λ_r denoted here as λ_r^* , we initially fix $\lambda_q = 1$ and plot the slopes m_i for different λ_r values, see Fig. A.1b. The line slopes m_i acquire various values while λ_r changes, but there is a value of λ_r , λ_r^* , at which all slopes are equal, i.e., $m_i \approx -0.5$:

$$\lambda_r^* = \frac{\sum_{s=1}^{n_s} |\mathcal{D}^{\text{fix},s}|}{|\mathcal{D}^{\text{free}}|}. \quad (\text{A.1})$$

Note that with this setting the slope of $\kappa_2(\mathbf{A}^{\text{eqb}})$ already reduces to zero, whereas $1/\det(\mathbf{A}^{\text{eqb}})$ monotonically increases at the rate $n_f/2$. This calls for the need to define the parameter λ_q .

The weighting factor λ_q can help tailor the unified m_i value at zero (rather than -0.5). Fig. A.1c sheds light on the influence of λ_q on the slopes m_i (while $\lambda_r = \lambda_r^*$) and therefore on the convergence behaviour of $1/\det(\mathbf{A}^{\text{eqb}})$. As evidenced in this plot, there exists a $\lambda_q = \lambda_q^*$ at which $m_i \approx 0$:

$$\lambda_q^* = \sqrt{\sum_{s=1}^{n_s} |\mathcal{D}^{\text{fix},s}| + |\mathcal{D}^{\text{free}}|}. \quad (\text{A.2})$$

Upon the consistent setting of the weighting parameters, the plots from Fig. A.1a are redrawn in Fig. A.1d. It is observed that all the mentioned quantities have become independent of the FE mesh, hence, $1/\det(\mathbf{A}^{\text{eqb}})$ and $\kappa_2(\mathbf{A}^{\text{eqb}})$ can be used as cost functions in the context of topology optimisation.

Appendix B. Other explored cost functions

This section discusses alternative cost definitions (explored for automated specimen design) and their pros and cons.

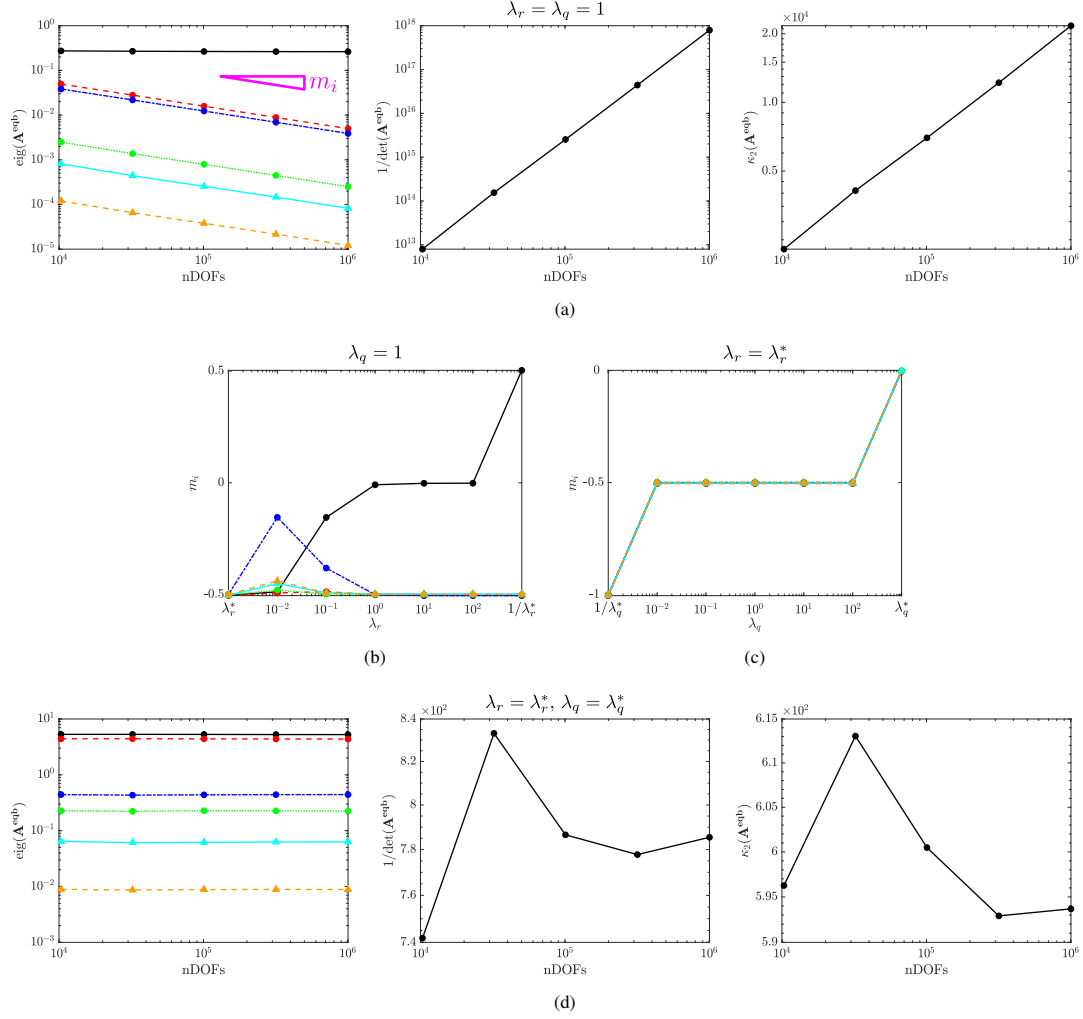


Figure A.1: Consistent definition of the weighting parameters λ_r and λ_q : (a) starting with $\lambda_r = \lambda_q = 1$ and plotting $\text{eig}(\mathbf{A}^{\text{eqb}})$ (sorted, each with a slope m_i), $1/\det(\mathbf{A}^{\text{eqb}})$ and $\kappa_2(\mathbf{A}^{\text{eqb}})$ versus nDOFs; (b) fixing $\lambda_q = 1$ and finding $\lambda_r = \lambda_r^*$ to unify the slopes m_i ; (c) fixing $\lambda_r = \lambda_r^*$ and finding $\lambda_q = \lambda_q^*$ such that the unified slopes m_i approach zero; (d) consistent values $\lambda_r = \lambda_r^*$ and $\lambda_q = \lambda_q^*$ lead to mesh-convergent behaviour. The eigenvalues and their corresponding slopes are in mm^2 , the determinant is in mm^{2n_f} , and the condition number is dimensionless.

B.1. Minimum distance between strain data points

One way to formulate the specimen design problem is by looking at the principal strain space and its coverage by the data points, i.e., strains at the Gauss points. The more widely and uniformly spread the data points, the richer the deformation field experienced by the specimen, and so, the more accurate the identified material parameters. In this context, a cost function based on the minimum distance between the strain data points can be defined as:

$$\text{cost}_{\text{alt},2} = - \left(\sum_{i=1}^{n(n-1)/2} \left(\frac{d_i}{\min(\mathbf{d}_{\text{@init}})} \right)^p \right)^{\frac{1}{p}}, \quad (\text{B.1})$$

where $\mathbf{d} \in \mathbb{R}^{n(n-1)/2}$ represents the vector containing all the unique pairwise Euclidean distances between n points in the principal strain space, and $\min(\mathbf{d}_{\text{@init}})$ denotes the minimum distance between the points at initialisation. The ℓ_p -regularisation term is used instead of the $\min(\cdot)$ operator to enable analytical differentiation.

Topology optimisation based on the cost in Eq. (B.1) aims at maximising the minimum distance between the data points, thus providing extensive coverage over the principal strain space. The advantage of such a cost definition

lies in the design of a specimen topology encompassing various deformation modes as it undergoes a simple uniaxial tensile test. On the other hand, the main downside of such a cost is its intrinsic *locality*, which only targets the minimum distance between the strain data points (i.e., a local feature), therefore lacking a *global* view of the whole design optimisation problem. Moreover, the minimisation of Eq. (B.1) would necessarily require a random field for initialisation with $\min(\mathbf{d}_{@init.}) > 0$, meaning that evenly distributed design densities (inducing concentrated and overlapping strain points) would be impractical.

B.2. Frobenius-norm condition number

An alternative to the 2-norm condition number is the condition number based on the Frobenius norm:

$$\kappa_F(\mathbf{A}^{eqb}) = \left\| \mathbf{A}^{eqb} \right\|_F \left\| \mathbf{A}^{eqb^{-1}} \right\|_F, \quad (\text{B.2})$$

where the Frobenius norm for \mathbf{A}^{eqb} with vectorised components A_i^{eqb} ($i = 1, \dots, n_f^2$) is given by

$$\left\| \mathbf{A}^{eqb} \right\|_F = \left(\sum_{i=1}^{n_f^2} \left| A_i^{eqb} \right|^2 \right)^{\frac{1}{2}}. \quad (\text{B.3})$$

It can be shown that the Frobenius norm of a matrix is always greater than or equal to its 2-norm (utilising Cauchy–Schwarz inequality). Thus the following bound relation can be found:

$$1 \leq \kappa_2(\mathbf{A}^{eqb}) = \left\| \mathbf{A}^{eqb} \right\|_2 \left\| \mathbf{A}^{eqb^{-1}} \right\|_2 \leq \left\| \mathbf{A}^{eqb} \right\|_F \left\| \mathbf{A}^{eqb^{-1}} \right\|_F = \kappa_F(\mathbf{A}^{eqb}). \quad (\text{B.4})$$

One can thus define the cost for topology optimisation based on $\kappa_F(\mathbf{A}^{eqb})$ as follows:

$$\text{cost}_{alt,3} = \frac{\kappa_F(\mathbf{A}^{eqb})}{\kappa_F(\mathbf{A}^{eqb}_{@init.})}, \quad (\text{B.5})$$

where $\kappa_F(\mathbf{A}^{eqb}_{@init.})$ denotes the Frobenius-norm condition number at initialisation. Even though κ_F is insensitive to the strain levels, we still normalise it by the corresponding value at the initial configuration; this is found to help increase the stability of the optimisation process (as pointed out earlier in Section 3). Unfortunately, the implementation of Eq. (B.5) in the optimisation framework leads to unstable behaviour of the optimiser and abrupt changes of the topology during the course of optimisation, to the extent that, in some cases, the output topology from one machine can vary slightly from the one of another machine. For this reason, we do not further use this cost definition.

B.3. p -norm condition number

The p -norm condition number in Eq. (18) is based on the matrix p -norm in Eq. (19). To establish a bound relation with respect to the Frobenius norm (and hence to the 2-norm), we leverage Hölder’s inequality for vectors \mathbf{a} and \mathbf{b} , with $r > 1$:

$$\sum_{i=1}^n |a_i| |b_i| \leq \left(\sum_{i=1}^n |a_i|^r \right)^{\frac{1}{r}} \left(\sum_{i=1}^n |b_i|^{\frac{r}{r-1}} \right)^{1-\frac{1}{r}}, \quad \forall \quad \mathbf{a}, \mathbf{b} \in \mathbb{R}^n \text{ or } \mathbb{C}^n, r > 1. \quad (\text{B.6})$$

By substituting $|a_i| = \left| A_i^{eqb} \right|^2$, $|b_i| = 1$ and $r = p/2 > 1$, and taking the square root, we obtain

$$\left(\sum_{i=1}^{n_f^2} \left| A_i^{eqb} \right|^2 \right)^{\frac{1}{2}} = \left\| \mathbf{A}^{eqb} \right\|_F \leq n_f^{1-\frac{2}{p}} \left(\sum_{i=1}^{n_f^2} \left| A_i^{eqb} \right|^p \right)^{\frac{1}{p}} = n_f^{1-\frac{2}{p}} \left\| \mathbf{A}^{eqb} \right\|_p. \quad (\text{B.7})$$

Such a bound relation can be obtained similarly for $(\mathbf{A}^{eqb})^{-1}$, giving the final inequality:

$$1 \leq \kappa_2(\mathbf{A}^{eqb}) \leq \kappa_F(\mathbf{A}^{eqb}) = \left\| \mathbf{A}^{eqb} \right\|_F \left\| \mathbf{A}^{eqb^{-1}} \right\|_F \leq n_f^{2(1-\frac{2}{p})} \left\| \mathbf{A}^{eqb} \right\|_p \left\| \mathbf{A}^{eqb^{-1}} \right\|_p = n_f^{2(1-\frac{2}{p})} \kappa_p(\mathbf{A}^{eqb}). \quad (\text{B.8})$$

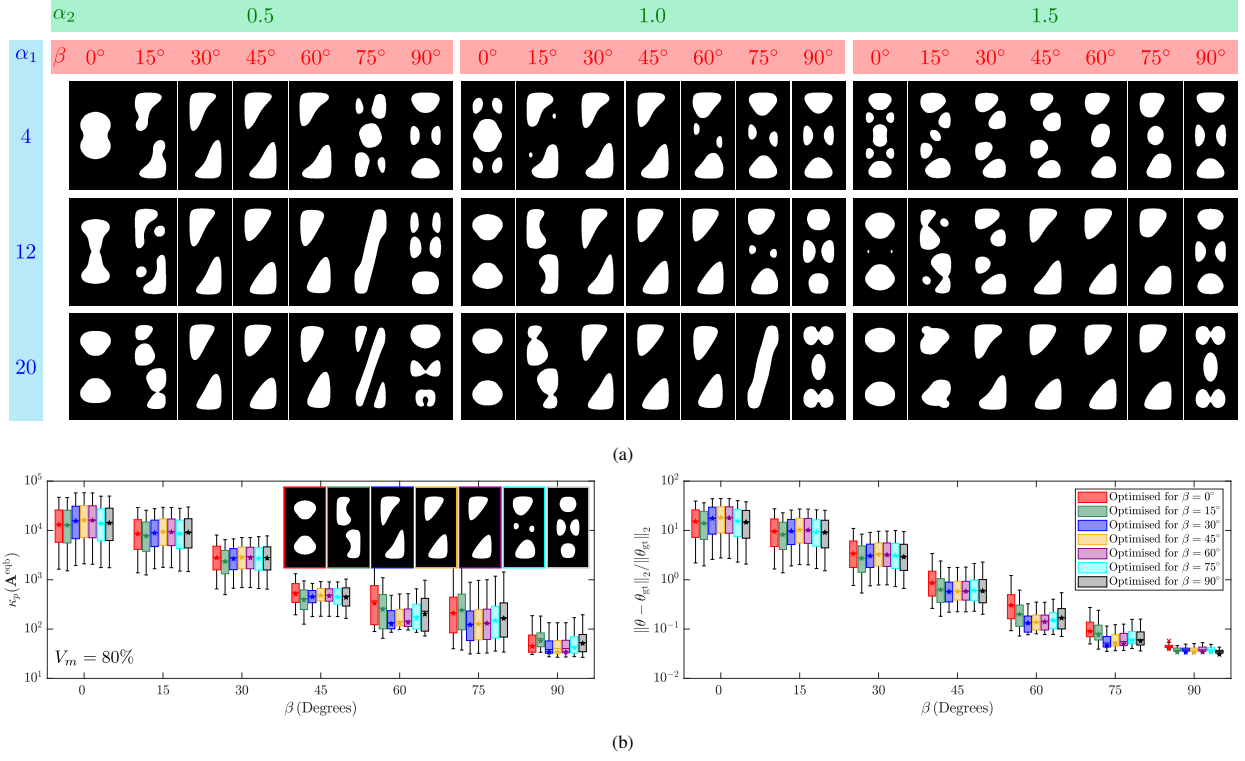


Figure B.1: The p -norm condition number as cost function: (a) optimised topologies with $p = 8$ for different orthotropic materials. The densities are initialised evenly, and the material volume constraint is set to $V_m = 80\%$; (b) identification of the orthotropic material parameters using the optimised topologies obtained with $(\alpha_1, \alpha_2) = (12, 1.0)$ from part (a). The left plot visualises the p -norm condition number (dimensionless) while the right one demonstrates the identification error (in percentage), both presented against the anisotropy angle β .

Therefore, the product $n_f^{2(1-\frac{2}{p})} \kappa_p(\mathbf{A}^{\text{eqb}})$ is an upper bound for $\kappa_F(\mathbf{A}^{\text{eqb}})$ which in turn is an upper bound for $\kappa_2(\mathbf{A}^{\text{eqb}})$.

The results for an isotropic material using κ_8 in Eq. (20) were already given in Fig. 4. Next, Fig. B.1a presents the results for orthotropic elasticity using the input material parameters in Table 1. The gallery of topologies is generated with the material volume fraction $V_m = 80\%$. The optimised topologies are rather similar to those obtained with the original determinant-based cost function (shown in Fig. 6). However, a few of the κ_8 -optimised topologies violate the special type of symmetry observed earlier in Fig. 6, see e.g. those obtained with $(\alpha_1, \alpha_2, \beta) = (12, 0.5, 90^\circ)$, $(20, 0.5, 15^\circ)$ and $(20, 0.5, 90^\circ)$. Moreover, narrow-width topological features are more frequent here, see e.g. $(\alpha_1, \alpha_2, \beta) = (4, 1.0, 15^\circ)$, $(12, 1.5, 0^\circ)$ and $(20, 1.0, 15^\circ)$. The performance of selected topologies generated via inputs $(\alpha_1, \alpha_2) = (12, 1.0)$ from the gallery is demonstrated in Fig. B.1b. The plots of cost and identification error visualise similar trends to their counterparts in Fig. 7, where the topology obtained with $\beta = 15^\circ$ is superior in terms of cost and identification error for many anisotropy orientations.

In view of the above, the cost function based on κ_p is not superior to the determinant-based cost function, hence, we do not further use it here.

Appendix C. Density filtering

As briefly discussed in Section 3.3, topology optimisation without regularisation is an ill-posed problem. For this reason, filtering techniques have been developed. Among the different choices proposed in the literature, a popular filtering technique is the so-called weight-averaged, density filtering over a neighbourhood of radius r_{\min} (Bruns and Tortorelli, 2001; Bourdin, 2001) which acts upon the design densities ρ_e as a convolution-type operator and transforms

them into the averaged densities

$$\rho_e^{\text{avg}} = \frac{1}{\sum_{i=1}^{n_e} H_{e,i}} \sum_{i=1}^{n_e} H_{e,i} \rho_i, \quad (\text{C.1})$$

with the convolution kernel

$$H_{e,i} = \max(0, r_{\min} - \Delta(e, i)). \quad (\text{C.2})$$

Here, $\Delta(e, i)$ denotes the distance between the centres of two elements e and i , which dictates how much the density of element i (within the neighbourhood r_{\min}) contributes to the averaged density of element e . The filtering radius r_{\min} is defined as

$$r_{\min} = \frac{r_{\min}^{\text{abs}}}{L_e}, \quad (\text{C.3})$$

with r_{\min}^{abs} as the absolute filtering radius and L_e as the element size. The ratio between the area of the absolute filtering neighbourhood $\pi(r_{\min}^{\text{abs}})^2$ and the domain area is kept constant and equal to $\bar{S}_{fd} = 0.15$ (see Fig. 2b). This setup leads to a mesh-independent filtering effect. The filtering radius r_{\min} dictates the minimum size of topological features allowed to form (in both material and void regions). There exists, however, a trade-off in setting r_{\min} (or equivalently \bar{S}_{fd}): in general, increasing r_{\min} results in broader averaging and stronger regularisation, hence larger topological features but also more grey scales; conversely, reducing r_{\min} gives rise to the formation of tiny features and checkerboard patterns with less grey scales in the optimised topology (see Fig. C.1). Therefore, a *sweet spot* can be found (most often with trial and error) which renders sufficiently large features and not many grey scales.

The convolution kernel can be pre-computed, assembled into a sparse matrix $\mathbf{H} \in \mathbb{R}^{n_e \times n_e}$, and then used throughout the optimisation process for matrix-vector multiplication with the vector of design densities. Here a twofold problem arises: first, when the filtering radius r_{\min} is increased for a bigger neighbourhood search (while keeping n_e constant), the computational complexity and the memory utilisation to compute \mathbf{H} grows quadratically for 2D problems; second, the number of nonzero entries in \mathbf{H} grows significantly (first linearly, and then almost logarithmically until saturation) which hinders the benefits of the sparse matrix-vector multiplication of \mathbf{H} with $\boldsymbol{\rho}$. To solve the memory issue explained above, we resort to the implicit filter proposed by Lazarov and Sigmund (2011). The density filtering in Eq. (C.1) is implicitly expressed by the solution of a Helmholtz-type PDE with homogeneous Neumann boundary conditions:

$$\begin{cases} -R_{\min}^2 \nabla^2 \rho^{\text{avg}} + \rho^{\text{avg}} = \rho, \\ \frac{\partial \rho^{\text{avg}}}{\partial \mathbf{n}} = 0, \end{cases} \quad (\text{C.4})$$

where ρ^{avg} and ρ are the continuous representations of the averaged and design densities, respectively, and $\mathbf{n} \in \mathbb{R}^2$ is the outward normal vector to the boundary. The parameter R_{\min} acts similarly to r_{\min} , with an approximate relation between them derived by Lazarov and Sigmund (2011):

$$R_{\min} = \frac{r_{\min}}{2\sqrt{3}}. \quad (\text{C.5})$$

Fig. C.1 illustrates the fairly similar behaviours of the PDE and convolution-type filters when they are applied to the same input noisy design field. The convolution-type filter regularises the topology more strongly, especially when \bar{S}_{fd} is relatively large. This is rooted in the definition of the approximate relation in Eq. (C.5).

As put forward by Lazarov and Sigmund (2011), the FE discretisation of the PDE in Eq. (C.4) can be formulated as a linear system with the solution $\boldsymbol{\rho}^{\text{avg}} \in \mathbb{R}^{n_e}$ as the weight-averaged densities:

$$\mathbf{K}_F (\mathbf{T}_F \boldsymbol{\rho}^{\text{avg}}) = (\mathbf{T}_F \boldsymbol{\rho}), \quad (\text{C.6})$$

where $\mathbf{K}_F \in \mathbb{R}^{|\mathcal{D}_F| \times |\mathcal{D}_F|}$ with $\mathcal{D}_F = \{(a, 1) : a = 1, \dots, n_n\}$ is the standard FE stiffness matrix for scalar problems (including the factor R_{\min}^2 in its definition), and $\mathbf{T}_F \in \mathbb{R}^{|\mathcal{D}_F| \times n_e}$ is a matrix that maps the element density values to a vector of respective nodal values. With this approach, the cost of filtering and the size of the involved matrices become independent of the filtering radius, which helps with memory usage reduction. However, the use of the PDE filter requires the solution of the additional FE problem in Eq. (C.6), which, however, can be achieved efficiently by

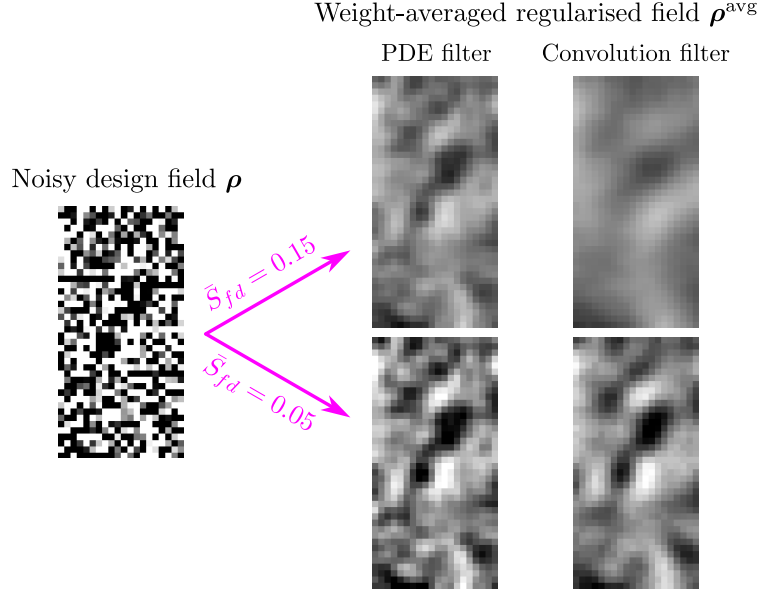


Figure C.1: Weight-averaged density filtering to regularise the topology optimisation problem: comparing the implicit PDE and explicit convolution-type filters for two different neighbourhood sizes defined by \tilde{S}_{fd} over a noisy design field.

one-time computation and storage of the factorisation of \mathbf{K}_F (refer to Andreassen et al. (2011) for implementation details).

As discussed earlier, density filtering produces intermediate density values, graphically represented as grey scales. Even though this is necessary for problem regularisation and convergence, grey scales are undesirable in the output topology since they cannot be manufactured in practice. To convert the grey-scaled into a black-and-white topology, techniques such as projection filtering have been introduced (Guest et al., 2004; Sigmund, 2007; Xu et al., 2010), see Wang et al. (2011) for a review. These projection filters can be applied on top of the density averaging schemes. In the simplest projection, if $\rho_e^{\text{avg}} \geq \phi$ (with ϕ as a chosen threshold) then the projected density, denoted as ρ_e^{phys} , becomes $\rho_e^{\text{phys}} = 1$, and if $\rho_e^{\text{avg}} < \phi$ then $\rho_e^{\text{phys}} = 0$. The projection given by

$$\rho^{\text{phys}} = \frac{\tanh(\psi\phi) + \tanh(\psi(\rho^{\text{avg}} - \phi))}{\tanh(\psi\phi) + \tanh(\psi(1 - \phi))} \quad (\text{C.7})$$

is a computationally efficient choice as it encodes the above threshold conditions in a vectorised expression. Here, ψ is a regularisation parameter. It is customary to start the optimisation process with $\psi = 2^0 = 1$ (i.e., almost no projection) to let the topology evolve freely, and to increase ψ gradually as the optimisation goes on. Andreassen et al. (2011) suggest to gradually double ψ with respect to the previous value whenever the stopping criterion is met until reaching $\tilde{\psi} = 2^9 = 512$, which approximately creates a step function that outputs binary designs. The stopping criterion is introduced in Section 3.5. Fig. 3 gives the flowchart of the optimisation algorithm where the continuation scheme for increasing ψ forms the outer loop. The threshold parameter ϕ in Eq. (C.7) is set to 0.5.

Appendix D. Analytical sensitivity calculation

Due to the employment of a gradient-based optimisation approach, we need to derive the analytical gradients (i.e., sensitivities) of the cost function with respect to the design variables ρ . Recalling the chain rule in Eq. (25), we find the three major derivatives here, namely $\frac{d(\text{cost})}{d\rho^{\text{phys}}} \in \mathbb{R}^{1 \times n_e}$, $\frac{d\rho^{\text{phys}}}{d\rho^{\text{avg}}} \in \mathbb{R}^{n_e \times n_e}$ and $\frac{d\rho^{\text{avg}}}{d\rho} \in \mathbb{R}^{n_e \times n_e}$:

(I) Derivation of $\frac{d(\text{cost})}{d\rho^{\text{phys}}}$

The sensitivity of the cost function in Eq. (21) with respect to the physical densities ρ^{phys} can be found from:

$$\frac{d(\text{cost})}{d\rho^{\text{phys}}} = \frac{\partial(\text{cost})}{\partial\rho^{\text{phys}}} + \frac{\partial(\text{cost})}{\partial\mathbf{U}} \frac{d\mathbf{U}}{d\rho^{\text{phys}}} . \quad (\text{D.1})$$

We start with the first term

$$\frac{\partial(\text{cost})}{\partial\rho^{\text{phys}}} = \frac{d(\text{cost})}{d\mathbf{A}_{\text{glob}}} \frac{\partial\mathbf{A}_{\text{glob}}}{\partial\rho^{\text{phys}}} , \quad (\text{D.2})$$

where

$$\frac{d(\text{cost})}{d\mathbf{A}_{\text{glob}}} = \frac{d(\text{cost})}{d\mathbf{A}^{\text{eqb}}} \frac{d\mathbf{A}^{\text{eqb}}}{d\mathbf{A}} \frac{d\mathbf{A}}{d\mathbf{A}_{\text{glob}}} , \quad (\text{D.3a})$$

$$\frac{d(\text{cost})}{d\mathbf{A}^{\text{eqb}}} = - \frac{\det(\mathbf{A}_{\text{@init.}}^{\text{eqb}})}{\det(\mathbf{A}^{\text{eqb}})} \underbrace{(\mathbf{A}^{\text{eqb}})^{-1}}_{\mapsto (1 \times n_f^2)} , \quad (\text{D.3b})$$

$$\frac{d\mathbf{A}^{\text{eqb}}}{d\mathbf{A}} = \left[\underbrace{\left(\frac{d\mathbf{A}^T}{d\mathbf{A}} \right)^T \mathbf{A}}_{\mapsto (n_f(|\mathcal{D}^{\text{free}}| + n_s) \times n_f^2)} \right]^T + \underbrace{\mathbf{A}^T \left(\frac{d\mathbf{A}}{d\mathbf{A}} \right)}_{\mapsto (n_f^2 \times n_f(|\mathcal{D}^{\text{free}}| + n_s))} , \quad (\text{D.3c})$$

$$\frac{d\mathbf{A}}{d\mathbf{A}_{\text{glob}}} = \frac{d\mathbf{A}}{d\mathbf{A}_{\text{glob}}^{\text{free}}} \frac{d\mathbf{A}_{\text{glob}}^{\text{free}}}{d\mathbf{A}_{\text{glob}}} + \frac{d\mathbf{A}}{d\mathbf{A}_{\text{glob}}^{\text{fix}}} \frac{d\mathbf{A}_{\text{glob}}^{\text{fix}}}{d\mathbf{A}_{\text{glob}}} , \quad (\text{D.3d})$$

and

$$\frac{\partial\mathbf{A}_{\text{glob}}}{\partial\rho^{\text{phys}}} = \bigcup_{e=1}^{n_e} 3(\rho_e^{\text{phys}})^2 (1 - \rho_{\min}) \underbrace{\mathbf{A}_e(\mathbf{U}_e)}_{\mapsto (|\mathcal{D}| n_f \times 1)} . \quad (\text{D.4})$$

In the equations above, we have introduced the operator $\mapsto (d_x \times d_y)$ to denote the reshaping of an array to $\mathbb{R}^{d_x \times d_y}$. In Eqs. (D.3c) and (D.3d) there are some remaining derivatives in the form of sparse constant matrices defined only once (at the first iteration) using the *sparse* operator in MATLAB, stored in the memory, and then used directly during the optimisation process. For brevity, we do not write these derivatives here.

Next, we compute the second term. For this, we first derive the state (i.e., equilibrium) equation in Eq. (22b) to find $\frac{d\mathbf{U}}{d\rho^{\text{phys}}} \in \mathbb{R}^{|\mathcal{D}| \times n_e}$ as follows

$$\frac{d\mathbf{K}}{d\rho^{\text{phys}}} \mathbf{U} + \mathbf{K} \frac{d\mathbf{U}}{d\rho^{\text{phys}}} = \mathbf{0} \Rightarrow \frac{d\mathbf{U}}{d\rho^{\text{phys}}} = -\mathbf{K}^{-1} \left(\frac{d\mathbf{K}}{d\rho^{\text{phys}}} \mathbf{U} \right) . \quad (\text{D.5})$$

This derivation requires solving a linear system with the right-hand side as the large matrix $\frac{d\mathbf{K}}{d\rho^{\text{phys}}} \mathbf{U} \in \mathbb{R}^{|\mathcal{D}| \times n_e}$ given by

$$\frac{d\mathbf{K}}{d\rho^{\text{phys}}} \mathbf{U} = \bigcup_{e=1}^{n_e} 3(\rho_e^{\text{phys}})^2 (1 - \rho_{\min}) \mathbf{K}_e(\boldsymbol{\theta}) \mathbf{U}_e . \quad (\text{D.6})$$

In order to avoid solving n_e systems of linear equations in Eq. (D.5), which is computationally expensive, we exploit the so-called *adjoint* method (i.e., backward derivation) (Johnson, 2012). Hence, we look for the product $\frac{\partial(\text{cost})}{\partial\mathbf{U}} \frac{d\mathbf{U}}{d\rho^{\text{phys}}}$, given by

$$\frac{\partial(\text{cost})}{\partial\mathbf{U}} \frac{d\mathbf{U}}{d\rho^{\text{phys}}} = - \underbrace{\frac{\partial(\text{cost})}{\partial\mathbf{U}} \mathbf{K}^{-1}}_{\gamma^T} \left(\frac{d\mathbf{K}}{d\rho^{\text{phys}}} \mathbf{U} \right) = -\gamma^T \left(\frac{d\mathbf{K}}{d\rho^{\text{phys}}} \mathbf{U} \right) , \quad (\text{D.7})$$

where we have introduced the adjoint vector $\boldsymbol{\gamma} \in \mathbb{R}^{|\mathcal{D}|}$ which is the solution to only *one* system of linear equations, i.e., the adjoint state equation

$$\mathbf{K}\boldsymbol{\gamma} = \left(\frac{\partial(\text{cost})}{\partial \mathbf{U}} \right)^T. \quad (\text{D.8})$$

The right-hand side of the adjoint system of equations is constructed by $\left(\frac{\partial(\text{cost})}{\partial \mathbf{U}} \right)^T \in \mathbb{R}^{|\mathcal{D}|}$ given by:

$$\frac{\partial(\text{cost})}{\partial \mathbf{U}} = \frac{d(\text{cost})}{d\mathbf{A}_{\text{glob}}} \frac{\partial \mathbf{A}_{\text{glob}}}{\partial \mathbf{U}}, \quad (\text{D.9a})$$

$$\frac{\partial \mathbf{A}_{\text{glob}}}{\partial \mathbf{U}} = \bigcup_{e=1}^{n_e} \tilde{\rho}_e^{\text{phys}} \underbrace{\frac{d\mathbf{A}_e(\mathbf{U}_e)}{d\mathbf{U}_e}}_{\mapsto (|\mathcal{D}_e|n_f \times |\mathcal{D}_e|)}, \quad (\text{D.9b})$$

$$\frac{d\mathbf{A}_e(\mathbf{U}_e)}{d\mathbf{U}_e} = \frac{d\mathbf{A}_e}{d\tilde{\boldsymbol{\varepsilon}}_e^f} \frac{d\tilde{\boldsymbol{\varepsilon}}_e^f}{d\boldsymbol{\varepsilon}_e^f} \frac{d\boldsymbol{\varepsilon}_e^f}{d\mathbf{U}_e} \approx \sum_{i=1}^{n_{\text{ep}}} \sum_{j=1}^{n_{\text{ep}}} \mathbf{B}_e^T(\xi_i, \eta_j) \underbrace{\frac{d\tilde{\boldsymbol{\varepsilon}}_e^f}{d\boldsymbol{\varepsilon}_e^f} \mathbf{B}_e(\xi_i, \eta_j) \det(\mathbf{J}_e(\xi_i, \eta_j))}_{\mapsto (3 \times n_f |\mathcal{D}_e|)} \times w_i \times w_j, \quad (\text{D.9c})$$

$$\frac{d\tilde{\boldsymbol{\varepsilon}}_e^f}{d\boldsymbol{\varepsilon}_e^f} = \begin{bmatrix} 1 & 0 & 0 & 0 & 1 & 0 & 0 & 0 & 1 & 0 & 0 & 0 & 0 & 0 & 0 & 0 & 0 & 0 \\ 0 & 0 & 0 & 1 & 0 & 0 & 0 & 0 & 0 & 0 & 1 & 0 & 0 & 0 & 1 & 0 & 0 & 0 \\ 0 & 0 & 0 & 0 & 0 & 0 & 1 & 0 & 0 & 0 & 0 & 0 & 0 & 1 & 0 & 0 & 0 & 1 \end{bmatrix}^T. \quad (\text{D.9d})$$

The adjoint method is beneficial since it enables the efficient computation of the sensitivities at the cost of solving only one extra linear system (whose cost is comparable to that of one FE analysis) rather than solving n_e linear systems.

(II) Derivation of $\frac{d\rho^{\text{phys}}}{d\rho^{\text{avg}}}$

The projection filter in Eq. (C.7) can be derived to obtain:

$$\frac{d\rho^{\text{phys}}}{d\rho^{\text{avg}}} = \text{diag} \left(\frac{\psi \text{sech}^2(\psi(\rho^{\text{avg}} - \phi))}{\tanh(\psi\phi) + \tanh(\psi(1 - \phi))} \right). \quad (\text{D.10})$$

The operator $\text{diag}(\cdot)$ creates a square diagonal matrix whose diagonal components are the entries of the input vector.

(III) Derivation of $\frac{d\rho^{\text{avg}}}{d\rho}$

Following the expression of the PDE filter in Eq. (C.6), it is possible to find:

$$\frac{d\rho^{\text{avg}}}{d\rho} = \mathbf{T}_F^T \mathbf{K}_F^{-1} (\mathbf{T}_F \mathbf{I}_{n_e}), \quad (\text{D.11})$$

where $\mathbf{I}_{n_e} \in \mathbb{R}^{n_e \times n_e}$ is the identity matrix.

Note that $\frac{d(\text{cost})}{d\rho}$ can be computed in a more efficient manner (Andreassen et al., 2011):

$$\frac{d(\text{cost})}{d\rho} = \left(\mathbf{T}_F^T \mathbf{K}_F^{-1} \left(\mathbf{T}_F \left(\left(\frac{d(\text{cost})}{d\rho^{\text{phys}}} \right)^T \cdot \left(\frac{\psi \text{sech}^2(\psi(\rho^{\text{avg}} - \phi))}{\tanh(\psi\phi) + \tanh(\psi(1 - \phi))} \right) \right) \right) \right)^T, \quad (\text{D.12})$$

with \cdot denoting the element-wise product of two vectors resulting in a vector with the same size.

The analytical computation of sensitivities would be more involved for more complex material behaviours (e.g., geometric/material non-linearities, dissipation). In such cases, one can resort to automatic differentiation. However, the principles of the adjoint method remain the same.

Appendix E. The effect of initialisation in the optimised topologies

As pointed out in Appendix C, our cost definition for topology optimisation is a non-convex and non-linear function of the design variables ρ . The non-convexity of the cost gives rise to the existence of numerous local minima in the high-dimensional space, which implies that the initial guess may significantly influence the reached solution, i.e., the obtained optimised design. In Section 4.2 we noticed that the topology optimised for a given anisotropy orientation β was not always the best for the identification of orthotropic materials with the same value of β . To dig further into this issue, we briefly examine the influence of the initial density field on the results of our topology optimisation framework.

Fig. E.1 illustrates the effect of initialisation in the optimised topologies and their performance in the identification of orthotropic materials. For conciseness, the results of this analysis are reported only for the material volume fraction $V_m = 90\%$ which led to the lowest identification error bounds among the different volume fractions shown in Fig. 7. Let us first look into the effect of noisy (rather than even) initialisations. To this aim, we generate noisy fields by perturbing the even density distribution with Gaussian noise with zero mean and 20% standard deviation, a sample of which is plotted in Fig. 2c. Further, in a multi-start setup, we create 50 different noise patterns (i.e., seeds), and feed them into the topology optimisation framework. For each anisotropy orientation β , the topology with the lowest (unnormalised) cost is selected as the optimal topology. Fig. E.1a visualises the optimised topologies obtained from the prescribed noisy initial fields together with their performance assessment graphs. As evident, the overall looks of the topologies are quite similar to the respective results from the evenly distributed initialisation (owing to the regularisation by the weight-averaged density filter), except for the topologies generated with $\beta = 0^\circ$ and 90° . Noisy-initiated optimised topologies, however, do not exhibit the special type of symmetry¹ originally observed in Fig. 6. Additionally, due to the introduction of noise, there exists a tendency for the formation of holes close to each other, which, as explained earlier, lowers the cost and the identification error. Also in these plots (and even to a larger extent than with even initialisation) we observe that optimised topologies with $\beta = 0^\circ$ and 75° lead to the best results almost in all cases. Possibly, following the procedure above but multi-starting with a much larger number of seeds (say 500), we could arrive at the expected situation where each β -optimised topology is the best for the identification of materials with that value of β . We did not try this. Otherwise, the robust topology optimisation approach showed promise to address this issue (see Section 4.3).

Fig. E.1b plots the results achieved by initialising the design field with the densities obtained after the first loop of optimisation (see Fig. 2d) for the inputs $(\alpha_1, \alpha_2, \beta) = (12, 1.0, 0^\circ)$ as an example. Since the "interim" densities are symmetric, the optimised topologies also turn out to be symmetric. We notice a quite different appearance of the topologies for almost all β angles, highlighting the crucial impact of the initial guess. Because of the significantly modified topologies, the costs and identification errors also perform quite differently than in the previous cases. Noteworthy is that no unique superior topology can be detected in this case.

Appendix F. Implementation aspects in MATLAB and computational performance

In this section, we report some details on the implementation aspects and the computational performance of the developed algorithm. Generally, topology optimisation aims at minimising a cost function dependent on a large number of design variables (in the order of $10^5 - 10^6$) through an iterative algorithm. Thus, the implementation must be efficient to ensure reasonable performance. In a MATLAB environment, it is essential that the cost and the sensitivities are computed in a highly vectorised fashion, thereby avoiding slow *for*-loops. When it comes to creating sparse matrices and performing assembly operations efficiently, the *sparse* operator in MATLAB is essential (Andreassen et al., 2011). The syntax reads $\mathbf{S} = \text{sparse}(\mathbf{i}, \mathbf{j}, \mathbf{v}, d_x, d_y)$ and generates the matrix $\mathbf{S} \in \mathbb{R}^{d_x \times d_y}$ from the triplets $\mathbf{i}, \mathbf{j}, \mathbf{v}$ such that $\mathbf{S}(\mathbf{i}(k), \mathbf{j}(k)) = \mathbf{v}(k)$ for any entry k (The MathWorks Inc., 2024c). Another implementation aspect is the use of the *memoize* command to cache the outputs of expensive functions and return the cached value (instead of its re-evaluation) given the function is called with the same inputs (The MathWorks Inc., 2024b). This functionality can be applied to the filtering operation since the filtered densities are required three times per iteration,

¹Noisy fields with standard deviations less than 15% are practically smoothened out with the application of the weight-averaged density filtering, hence, they often produce symmetric results resembling those obtained with the even initialisation.

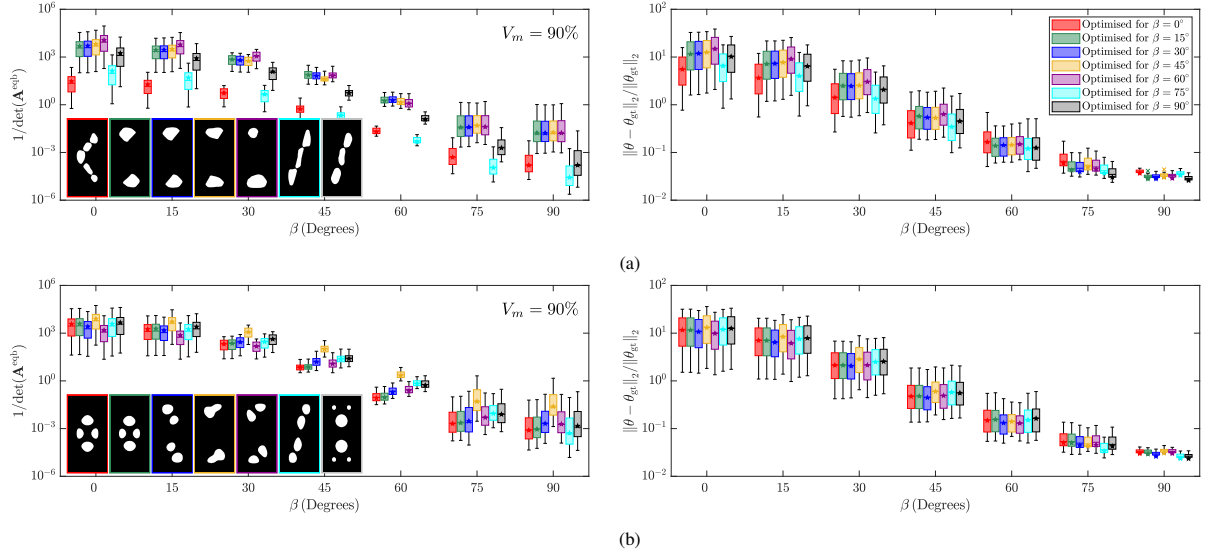


Figure E.1: The effect of initialisation on the optimised topologies, the unnormalised cost (in mm^{-12}) and the identification error (in percentage) (shown only for $V_m = 90\%$ for brevity): (a) initialisation with 20% noise in design densities, illustrated in Fig. 2c; (b) initialisation from the interim result of $\beta = 0^\circ$, illustrated in Fig. 2d. These results are comparable to those from initialisation with evenly distributed densities in Fig. 7(c).

namely, to compute the cost and the constraint and to plot the evolving topology. This is inevitable since sharing the filtered densities at each iteration of the optimisation loop among different functions is not straightforward in MATLAB.

To gain more efficiency in the optimisation framework, many constant FE- and cost-related calculations (partly thanks to the fixed structured mesh) need to be executed only once at the beginning and then stored in the memory as persistent variables to be readily available throughout the optimisation process. The same practice can be followed to precompute and cache large constant sparse matrices as well as the position vectors \mathbf{i} and \mathbf{j} for variable-valued sparse matrices. Note that position vectors can be stored as single-precision arrays to decrease the memory footprint. As pointed out in Appendix D, to efficiently compute the sensitivities of the cost with respect to the design variables, the adjoint method should be employed which requires one additional FE-like system of equations instead of n_e . Also, with the use of the PDE filter rather than the convolution-type operation, the memory usage is reduced substantially since the problem size and complexity of the former do not depend on the filtering radius.

Building on the implementation aspects discussed above, our topology optimisation algorithm for optimal specimen design with 157922 design variables (i.e., the converged discretisation level) runs in about 6 hours on a desktop machine with Core i7 3.8 GHz processor, requiring only 8 GB of random access memory throughout the computations. When using the robust formulation, the wall-clock time roughly reaches 14.5 hours, whereas parallelisation over three processors speeds up the algorithm by nearly 24% resulting in a run time of approximately 11 hours. Investigating the optimisation process, it is revealed that the MATLAB optimiser engine *fmincon* sometimes requires too many cost evaluations to solve the saddle-point problem (i.e., the Karush-Kuhn-Tucker conditions) and to compute the search direction in each iteration (Rojas-Labanda and Stolpe, 2015). To improve the temporal performance, it might be helpful to try other available optimiser engines, which require fewer function evaluations per iteration, e.g. the method of moving asymptotes (Svanberg, 1987).